Effect of a modulated acoustic field on the dynamics of a vibrating charged bubble

O. T. Kolebaje[b,a], U. E. Vincent[b,c,*], B. E. Benyeogor[b], P. V. E. McClintock[c]

[a] *Department of Physics, Adeyemi Federal University of Education, Ondo, Ondo State, Nigeria.*
[b] *Department of Physical Sciences, Redeemer's University, P.M.B. 230, Ede, Nigeria.*
[c] *Department of Physics, Lancaster University, Lancaster LA1 4YB, United Kingdom.*

Abstract

We investigate the effect of amplitude-modulated acoustic irradiation on the dynamics of a charged bubble vibrating in a liquid. We show that the potential $V(x)$ of the bubble, and the number and stability of its equilibria, depend on the magnitude of the charge it carries. Under high-frequency amplitude-modulation, a modulation threshold, G_{th}, was found for the onset of increased bubble amplitude oscillations. For some pressure field values, charge can facilitate the control of chaotic dynamics via reversed period-doubling bifurcation sequences. There is evidence for peak-shouldering and shock waves. The Mach number increases rapidly with the drive amplitude G. In the supersonic regime, for $G > 1.90$ Pa, the high-frequency modulation raises both Blake's and the transient cavitation thresholds. We found a decrease in the bubble's maximum charge threshold, and threshold modulation amplitude for the occurrence Vibrational resonance (VR). VR occurs due to the modulated oscillatory pressure field, and the influence on VR of the electrostatic charge, and other parameters of the system are investigated. In contrast to the cases of VR reported earlier, where the amplitude G of the high-frequency driving is typically much higher than the amplitude of the low-frequency driving (P_s), the VR resonance peaks occur here at relatively low G values ($0 < G < 10$ Pa) compared to the acoustic driving pressure $P_s \sim 10^5$ Pa. The optimal parameter values for enhanced response could be useful in acoustic cavitation applications.

Keywords: Bubble oscillator, amplitude modulation, acoustic waves, electrostatic charges, vibrational resonance

1. Introduction

Bubbles are nonlinear oscillators that exhibit variety of intriguing and complex dynamical properties. Research on bubble dynamics and its potential applications dates back more than a century to the work of Lord Rayleigh [1], seeking to minimise damage to ships' propellers. Since then, scientific and technological interest in bubbles has increased tremendously [2]. It is largely the numerous emerging applications that motivate the continuing intense research interest in bubble dynamics.

The dynamics of driven bubbles is relevant to a broad range of investigations. The emergence of such studies, more than four decades ago, quickly made driven bubbles prototypical examples of driven nonlinear systems that exhibit rich dynamical behaviour, becoming ubiquitous within the nonlinear dynamics research community [2, 3]. The driving force often arises from external influences of either deterministic (e.g. periodic or aperiodic) [3–5] or stochastic (i.e. noisy inputs) origin [3, 5, 6]. In some applications related to acoustic cavitation, such as in sonochemical reactors [7], fluid engineering, and medical diagnostics and therapy [8], multi-frequency driving acoustic sound waves, consisting of two or more input forces with distinct or identical frequency components, are often engineered into a bubble system as control inputs. In addition to the plethora of intriguing dynamical properties found in single-frequency oscillators, phenomena such as *mixed-mode oscillation, i.e. bursting* [9–12], *combination* and *simultaneous resonance* [13] and *vibrational resonance* (VR) [8, 14] may appear under different dual-frequency acoustic driving conditions. Dual-frequency forces can promote the acceleration of bubble growth via mass transfer, thereby leading to the generation of large bubbles [15]. Moreover, the combination of dual-frequency ultrasound irradiation and multiple-triggered high-intensity focused ultrasound (HIFU) was shown to be more efficient than conventional triggered HIFU for cavitation bubble cloud generation and expansion. More recently, it was shown that the dual-frequency excitations: (i) enhance the cavitation dynamics and associated stress/strain more efficiently [16]; (ii) promote increased sonochemical yields [17]; (iii) promote a higher negative-pressure amplitude than that of single-frequency ultrasound, which is more appropriate for the generation of cavitation [18]; and (iv) enable the clear distinction of cavitation sequences based on phase differences, which has potential applications in ultrasonic cavitation micromanipulation [18]. In addition, ultrasound-assisted freezing employing multi-frequencies

*Corresponding author
Email address: u.vincent@lancaster.ac.uk (U. E. Vincent)

improved significantly the freezing rate, maintained the myofibrillar structure, and reduced lipid oxidation [19].

In all earlier investigations of the effect of dual-frequency driving on bubbles, the model bubbles were uncharged to the best of our knowledge. However, it has been shown that, when irradiated by acoustic fields, air and gas bubbles in liquids are in practice electrostatically charged. Charge deposition on bubbles at bubble-liquid interfaces is a problem of long standing [20–22]. The phenomenon has been confirmed experimentally to be connected to the migration of ionic charge from the liquid onto the bubble surface [23]. Despite the many potential applications of charged bubbles – e.g. the production of electro-aerosol sprays which are composed of highly charged particles [24], biomedicine [25], water treatment [26], and food production [27] – the dynamics of driven charged bubbles has yet to be fully understood. Notable contributions were made, however, by Hongray et al. [28, 29] and Ashok et al. [30], using the modified Rayleigh-Plesset equation for an acoustically single-frequency driven gas bubble while considering the presence of charge q on the surface of the bubble. Hongray et al. [28, 29] and Ashok et al. [30] reported that the presence of charge reduces the effective surface tension of the bubble, thereby causing the charged bubble to expand to a larger radius and consequently undergo violent collapse to a minimum radius, as well as lowering the Blake's threshold [28]. In addition, Hongray *et al* [29] reported that the presence of charge advances the occurrence of the period-doubling-bifurcations route to chaos and increases the maximum attainable bubble radius.

The VR phenomenon has become one of the most prominently investigated resonance phenomenon in recent times owing to the numerous potential applications highlighted in Ref. [31]. It can manifest when the frequency components (say, Ω and ω) are chosen appropriately such that $\Omega \gg \omega$, where Ω is considered to be much faster with respect to ω. Succinctly, VR is the enhancement of the response of a system through the cooperation between two periodic driving signals whose frequencies differ substantially. Since VR was proposed over two decades ago [32], several model systems have been investigated and their applications explored [5, 8, 33–40]. Rapid progress has been made, both theoretically and experimentally [41–49, 49]. In recent papers by some of us [8, 14], the uncharged Rayleigh-Plesset (R-P) bubble model moving in an incompressible liquid was considered without any attention to the possible impact of the modulation on other dynamical properties of the bubbles, such as the Mach number, bifurcations, phase space trajectories and attractors in the Poincaré section. It is well-known that the R-P model is inappropriate when dealing with the large-amplitude oscillations often encountered during certain biomedical applications. Consequently, in this paper, we consider a charged bubble moving in a compressible liquid while driven by amplitude-modulated acoustic waves. The model is therefore a modified R-P equation [28, 29]. In addition to exploring the impact of the amplitude modulation on the charged bubble dynamics, we focus on the impact of charge on the VR phenomenon. In doing so, we obtain for the first time the potential $V(x)$ for a charged bubble and show that its nature, and the number and stability of its equilibria, will depend on the magnitude of the charge. We report high-frequency amplitude-modulation-induced peak-shouldering, shock waves and a rapidly-increasing Mach number, as well as control of chaotic regimes through cooperation between electrostatic charges and modulation. We also observe shifts in the bubble's characteristic pressure thresholds due to the vibrational effects of the high-frequency amplitude modulation. Finally, we establish the occurrence VR, and we explore the impacts of the electrostatic charge, the equilibrium radius, the parameters of the acoustic driving field, and the surface tension.

The rest of this paper is structured as follows: In Section 2 we present the charged bubble model and express it as the dynamics of a classical particle in a potential well [8, 50]. We explore the potential structure and discuss the dependence of the stability of equilibrium points on the magnitude of the charge q. In Section 3, numerical simulation results are presented and discussed, with emphasis on the effects of amplitude-modulation on the bubble dynamics as well as the effects of charge, driving pressure, equilibrium radius, and surface tension on VR. We summarise and draw conclusions in Section 4.

2. Model

We start from the equation for an uncharged gas bubble of radius R and equilibrium radius R_0 oscillating in water. Assuming no shape deformations, no angular oscillations or translational motion, the radial equation of motion is given by [28]:

$$\left(1-\frac{\dot{R}}{c}\right)R\ddot{R}+\frac{3}{2}\dot{R}^2\left(1-\frac{\dot{R}}{3c}\right)=\left(1+\frac{\dot{R}}{c}\right)\frac{P}{\rho}+\frac{R}{\rho c}\frac{dP}{dt}, \tag{1}$$

where

$$\begin{aligned} P &= \left(P_0-P_v+\frac{2\sigma}{R_0}\right)\left(\frac{R_0}{R}\right)^{3\Gamma}-\frac{2\sigma}{R}-4\eta\frac{\dot{R}}{R}-P_{stat} \\ &\quad +P_v-P_s(1+G\sin\Omega t)\sin\omega t, \end{aligned} \tag{2}$$

is the total pressure exerted on the bubble, c is the speed of sound in the fluid, ρ is its density, η is its viscosity, σ is its surface tension, P_0 is the pressure, P_v is the vapour pressure and Γ is the polytropic index of the gas inside the bubble. The term containing $\left(\left(1-\frac{\dot{R}}{c}\right)\right.$ defines the compressibility of the liquid.

The last term in Eq. (2) is the acoustic driving pressure field of frequency ω and amplitude P_s, modulated by a high-frequency field $G\sin\Omega t$, where G and Ω are the modulation amplitude and frequency, respectively. In industrial applications of cavitation and single bubble sonoluminescence (SBSL) wherein bubbles emit light when irradiated

by a high-frequency modulating acoustic signal, only certain parameters are tunable. The high-frequency modulation signal is usually regarded as the most appropriate, since in practice we can only expect to adjust the parameters of the external acoustic signal. For example, during high-intensity focused ultrasound (HIFU) treatment for a tumor, it would be impracticable to open up the skin to alter the properties of the tumor medium [51]. This justifies our choice of acoustic modulation to control the bubble dynamics.

To consider the effect of electrostatic charges on the bubble model, the charged bubble is regarded as a non-conducting charged spherical shell with a constant charge q on its surface. The presence of charge q on the bubble's surface reduces the effective value of the surface tension σ. To account for this, an electrostatic pressure field term $P_q = q^2/(8\pi\epsilon R^4)$ generated by a charge q may be included in the pressure balance equation at the bubble wall, where ϵ is the permittivity of the dielectric space-filling liquid. The pressure, P_q for a charged spherical bubble in dielectric fluid was derived by Grigor'ev and Zharov [52], and employed by Hongray et al. [28, 29]. Thus, Eq. (1) now becomes

$$\begin{aligned}\left[\left(1-\frac{\dot{R}}{c}\right)R+\frac{4\eta}{c\rho}\right]\ddot{R} &= \frac{1}{\rho}\left(P_0-P_v+\frac{2\sigma}{R_0}-\frac{q^2}{8\pi\epsilon R^4}\right)\\ &\times\left(\frac{R_0}{R}\right)^{3\Gamma}\left(1+\frac{\dot{R}}{c}(1-3\Gamma)\right)-\frac{\dot{R}^2}{2}\left(3-\frac{\dot{R}}{c}\right)\\ &+\frac{q^2}{8\pi\rho\epsilon R^4}\left(1-\frac{3\dot{R}}{c}\right)-\frac{2\sigma}{\rho R}-\frac{4\eta}{\rho}\left(\frac{\dot{R}}{R}\right)\\ &-\frac{1}{\rho}[P_0-P_v+P_s(1+G\sin\Omega t)\sin\omega t]\left(1+\frac{\dot{R}}{c}\right)\\ &-\frac{R}{\rho c}\left[\omega P_s(1+G\sin\Omega t)\cos\omega t+\Omega P_s G\sin\omega t\cos\Omega t\right]. \quad (3)\end{aligned}$$

We now seek an exact expression for the potential function of a charged bubble governed by Eq. (3). This analysis is important in order to elucidate the structure of the potential in which the charged bubble oscillates, and to explore the stability of the equilibrium state(s) and how the presence of charge affects them. The procedure to be employed is adapted from Refs. [8, 14], which is an improved version of the linear oscillation approach employed by Zhang [53] and Hamaguchi and Ando [54]. However, it has the advantage of retaining the higher-order nonlinear terms of the oscillator. In the formulation, we assume only radial oscillations, and express the bubble radius R in terms of its expansion or contraction variable x, taken to be dimensionless. So $R = R_0(1 + x)$ and by substituting it into the charged bubble equation for the case where $G = 0$ Pa (in the absence of the high-frequency modulation), Eq. (3) then becomes (See the Appendix 1 for details)

$$\begin{aligned}\ddot{x}+\dot{x}\left[\alpha_0+\alpha_1 x+\alpha_2 x^2+\alpha_3 x^3\right]+\frac{3}{2\phi}\dot{x}^2(1-x+x^2)\\ +\frac{\lambda}{2\phi}\dot{x}^3(1-x+x^2)+\frac{dV(x,t)}{dx}\\ =\frac{P_s\lambda\omega}{\phi\rho R_0^2}\cos\omega t-\frac{P_s}{\phi\rho R_0^2}\sin\omega t, \quad (4)\end{aligned}$$

where the potential is

$$V(x,t)=\frac{\gamma_1}{2}x^2+\frac{\gamma_2}{3}x^3+\frac{\gamma_3}{4}x^4. \quad (5)$$

The parameters $\alpha_i (i = 0, 1, 2, 3)$ and $\gamma_i (i = 1, 2, 3)$ given in Eqn. (19) and (20) (see Appendix 1) are the damping and potential parameters, respectively – all of which are charge-dependent. $\lambda = -\frac{R_0}{c}$, and $\phi = 1+\frac{1}{\rho R_0 c}$ arises from the compressibility term. By considering γ_1 from Eqn. (20) and dropping higher-order damping terms in $\alpha_i (i = 1, 2, 3)$ given by Eqn. (19) for the unforced oscillator, it is easy to recover the expressions for the linear natural frequency and the linear damping of the oscillator obtained by Hongray *et al.* [28]. Indeed, our model preserves the nonlinearity of the bubble oscillator up to third-order in its expansion or contraction, thus, making for more elegant and accurate analysis of the system's stability compared to the work of Grigor'ev and Zharov [52].

In the absence of the external acoustic field, the potential $V(x, t)$ becomes dependent only on position, as $V(x)$. The nature of the potential $V(x)$, and the number and stability of its equilibria will depend on the parameters of the charged bubble, and especially on the magnitude of the charge q that it carries. We now proceed to discuss the equilibria of this potential and the nature of their stability. The three possible equilibria of the potential obtained from solving $dV/dx = 0$ are

$$x_1 = 0, \qquad x_{2,3} = \frac{-\gamma_2 \pm \sqrt{\gamma_2^2 - 4\gamma_1\gamma_3}}{2\gamma_3}.$$

The unperturbed charged bubble oscillator can be written as

$$\begin{aligned}\dot{x} &= y\\ \dot{y} &= -\gamma_1 x-\gamma_2 x^2-\gamma_3 x^3. \quad (6)\end{aligned}$$

The Jacobian matrix J is

$$J=\begin{pmatrix}0 & 1\\ \chi & 0\end{pmatrix} \quad (7)$$

where $\chi = -\gamma_1 x - 2\gamma_2 x - 3\gamma_3 x^2$. The eigenvalues of J are given by $\pm\sqrt{\chi}$. Hence, if $\chi > 0$, the equilibrium is a saddle point; it is a stable center for $\chi < 0$.

Figure 1 plots the dependence of the equilibria of the system's potential on the magnitude of the charge q. We now discuss these results which, for convenience, are summarized in Table 1. For $q < 0.717$ pC, the potential is

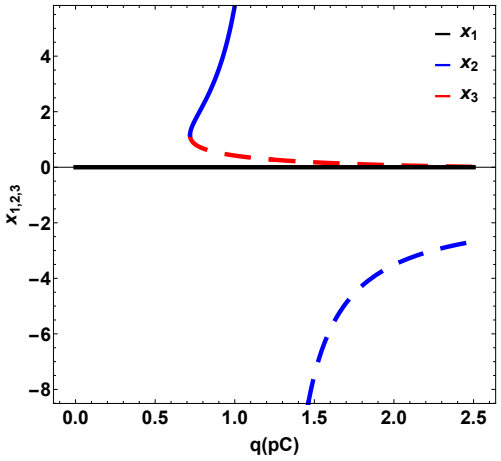

Figure 1: The bifurcation diagram of the equilibrium point, showing the appearance of three equilibria $x_{1,2,3}$ of the system computed from the potential $V(x)$ with the variation in bubble charge q in pC. The Dashed lines indicate instability of the equilibria while the solid lines indicate stable equilibria. The parameter values are $\Gamma = 5/3$, $\rho = 998$ kgm^{-3}, $\eta = 10^{-3}$ Nsm^{-2}, $c = 1500$ ms^{-1}, $P_v = 2.34$ kPa, $P_0 = 101$ kPa, $\sigma = 0.0725$ Nm^{-1}, $\epsilon = 85\epsilon_0$, where ϵ_0 is the permittivity of vacuum.

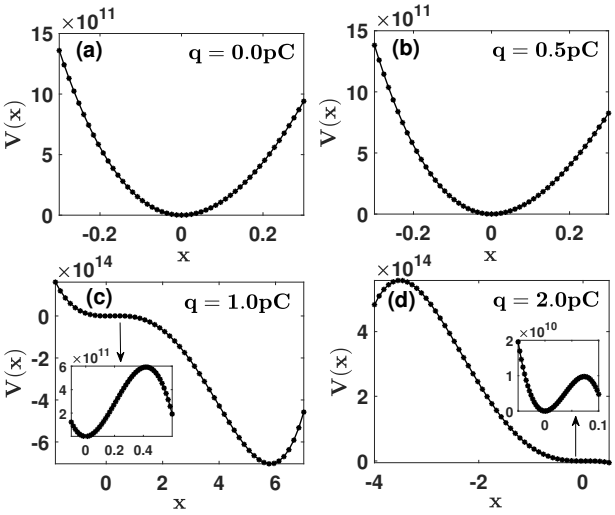

Figure 2: The potential $V(x)$ of the charged bubble in Eq. (5) for (a) $q = 0.0$ pC (single-well); (b) $q = 0.5$ pC (single-well); (c) $q = 1.0$ pC (double-well); and (d) $q = 2.0$ pC (single-well double-hump). Other parameters were fixed as in Figure 1

a single-well with a stable equilibrium always at $x = 0$ denoted by the solid black line. The potential is a double-well from $q = 0.717$ pC to about 1.45 pC, after which it becomes a single-well with a double-hump. The well at $x = 0$ collapses into the right hump when $q > 1.45$ pC, leading to an instability in the potential structure. This instability is consistent with the maximum charge threshold for bubbles previously established by Hongray *et al.* [28, 29]. Figure 2 depicts the dependence of the structure and shape of the potential $V(x)$ on the charge (q) of the bubble. For the parameters used here, the potential $V(x)$ of an uncharged bubble is an asymmetrical single-well centered around $x = 0$. At $q = 0.5$ pC and up to about 0.717 pC, the potential remains a single-well, as illustrated in Figure 1. The potential at $q = 1.0$ pC is an asymmetric double-well, with the right-well significantly deeper than the left-well located at $x = 0$. The potential at $q = 2.0$ pC is a single-well located at $x = 0$ with double humps on either side. The left hump potential barrier, located at $x < 0$, is significantly higher than the right hump potential barrier, located at $x > 0$. In this case, as the charge q exceeds 1.45 pC, the particles of the charged bubble system gain sufficient energy to overcome the appropriate potential barriers, resulting in the observed instability in the charged bubble dynamics.

3. Results and discussion

The results presented here were obtained from numerical solutions for the charged bubble in Eq. (3), rewritten as a set of coupled first-order autonomous ordinary differential equations (ODEs). Let $x = R$, $y = \dot{R}$ and

$$z_1 = \frac{1}{\rho}\left(P_0 - P_v + \frac{2\sigma}{R_0} - \frac{q^2}{8\pi\epsilon R^4}\right) R_0^{3\Gamma},\ z_2 = \frac{1-3\Gamma}{c},$$
$$z_3 = \frac{q^2}{8\pi\rho\epsilon},\ z_4 = \frac{2\sigma}{\rho},\ z_5 = \frac{4\eta}{\rho},\ z_6 = \frac{P_0 - P_v}{\rho},$$
$$z_7 = \frac{P_s}{\rho},\ z_8 = \frac{P_s\omega}{\rho c},\ z_9 = \frac{P_s\Omega}{\rho c},\ z_{10} = \frac{4\eta}{\rho c}. \quad (8)$$

Then Eq. (3) can be written as

$$\dot{x} = y, \qquad \dot{y} = \psi_1\psi_2, \quad (9)$$

where

$$\psi_1 = \frac{z_1}{x^{3\Gamma}}(1 + z_2 y) - \frac{y^2}{2}\left(3 - \frac{y}{c}\right) + \frac{z_3}{x^4}\left(1 - \frac{3y}{c}\right)$$
$$-\frac{z_4}{x} - \frac{z_5 y}{x} - \Delta_1(t)\left(1 + \frac{y}{c}\right) - x\Delta_2(t),$$

$$\psi_2 = \left[\left(1 - \frac{y}{c}\right)x + z_{10}\right]^{-1},$$

and

$$\Delta_1(t) = z_6 + z_7(1 + G\sin\Omega t)\sin\omega t,$$
$$\Delta_2(t) = z_8(1 + G\sin\Omega t)\cos\omega t + z_9 G\sin\omega t\cos\Omega t.$$

Equation (9) is then solved numerically by implementation in MATLAB-Simulink with the initial conditions $x(0) = R(0) = R_0 = 5.0$ μm, $y(0) = \dot{R}(0) = 0$. Simulink is a MATLAB-based environment for modelling and simulating dynamical systems [44]. We choose $\Gamma = 5/3$, corresponding to an adiabatic heat transfer process across the bubble surface. Except where otherwise indicated, the parameters of the model are fixed at $P_v = 2.34$ kPa,

Table 1: Summary of the effect of charge on the system equilibria.

Quantity of charge, q (pC)	Stability Property
$q < 0.717$	Stable single equilibrium (at $x = 0$)
$0.717 \leq q \leq 1.0$	Three equilibria: 2 stable (at $x = 0$ and $x > 0$), 1 unstable
$1.0 < q \leq 1.5$	Two equilibria: 1 stable (at $x = 0$), 1 unstable (at $x > 0$)
$q > 1.5$	Three equilibria: 1 stable (at $x = 0$), 2 unstable (at $x < 0$ and $x > 0$)

ν (linear frequency) = 10 kHz, $\omega = 2\pi\nu = 62.83$ kHz, $\Omega = 5.0\omega$, $P_s = \kappa P_0$, $\rho = 998$ kg m^{-3}, $\eta = 10^{-3}$ Ns m^{-2}, $c = 1500$ ms^{-1}, $P_0 = 101$ kPa, $\sigma = 0.0725$ Nm^{-1}, $\epsilon = 85\epsilon_0$, where ϵ_0 is the permittivity of the vacuum.

The bubble's response to the acoustic signal of frequency ω can be computed numerically from the expression

$$Q = \frac{\sqrt{Q_S^2 + Q_C^2}}{P_s}, \tag{10}$$

where Q_s and Q_c are related to the Fourier sine and cosine spectra of the time series of the output signal $R(t)$, respectively, and expressed as

$$Q_s = \frac{2}{nT}\int_0^{nT} R(t)\sin\omega t dt, \tag{11}$$

$$Q_c = \frac{2}{nT}\int_0^{nT} R(t)\cos\omega t dt. \tag{12}$$

$T = \frac{2\pi}{\omega}$ is the period of oscillations of the input signal frequency ω and $n = 1, 2, 3, \ldots$ is the number of complete oscillations.

3.1. Effect of amplitude modulation on the bubble dynamics

We now describe some effects of the amplitude modulation by the high-frequency field $G\sin\Omega t$ on the dynamics of the charged bubble. Figure 3 plots R/R_0 as a function of the driving periods (3 driving periods) at $G = 0$ Pa, 0.30 Pa and 0.60 Pa. The periods 100-103 were chosen to ensure that the system had reached a steady state solution. As previously reported by Hongray *et al.* [28], the maximum and minimum radii attainable by a charged bubble increase and decrease, respectively, when compared to an uncharged bubble. In the absence of high-frequency amplitude modulation, the bubble exhibits small-amplitude stable oscillations, and the bubble radial amplitude can only increase to about 1.3 times the equilibrium radius R_0, as shown in Fig. 3 (middle panel). For small amplitude ($G = 0.3$ Pa) of the high-frequency modulation, there is no significant difference in the maximum attainable bubble radius from the case $G = 0$ Pa; however, the time-series maxima are split into two distinct and equal peaks (peak shouldering) (Figure 3, upper panel). The lower panel of Figure 3 shows that the time-series maxima split into two distinct but unequal peaks as the high-frequency modulation amplitude $G = 0.60$ Pa increases further. The maximum radius attained by the bubble in this case is approximately twice or 2.5 times the equilibrium radius R_0 for the neutral or charged bubbles, respectively, when $q = 0.80$ pC. When $G = 0.60$ Pa, bursting-like spikes (shock waves) appear in the radial time evolution. These emitted shock waves are often associated with a strong collapse of the bubble after expansion, and they transport significant portions of the bubble's energy into the liquid, resulting in weak after-bounces due to strong damping [2]. Detailed characteristics of the bursting dynamics, which are beyond the scope of the present paper, are in general dependent on the ratio between the frequencies Ω and ω and will be reported elsewhere. Plots of the maximum radius attainable by the bubble as a function of the modulation amplitude G for neutral and charged bubbles are shown in Figure 4(a). We found that increasing G from zero to 0.5 Pa results in a very small change in the amplitude of the oscillation. Notably, a small increase in G beyond $G = 0.5$ Pa, impacts significantly on the amplitude of the bubble oscillatory dynamics. At $G = 0.50$ Pa precisely, the maximum radii attainable by the bubble are 1.58 and 1.67 times the equilibrium radii for the neutral and charged bubbles, respectively, for fixed $q = 0.80$ pC. For the same quantity of charge at $G = 1.00$ Pa, however, the maximum radius of the bubble rapidly increases to 7.00 and $7.15 \times R_0$ for the neutral and charged bubbles, respectively. Thus, increase in the high-frequency modulation amplitude increases the amplitude of the bubble oscillation. However, it is counter-intuitive that the relationship between the high-frequency modulation and amplitude of the bubble oscillation is nonlinear in nature.

Figure 5 shows a plot of the Mach number as a function of driving period (3 driving periods) and the corresponding spectral analysis of the time series at $G = 0$ Pa, 0.30 Pa and 0.60 Pa. The Mach number [55, 56], denoted by $\dot{R}/c$ in the current application, is a dimensionless quantity that represents the ratio of a body's speed to the speed of sound in the surrounding medium. The Mach number regimes are classified as subsonic ($\dot{R}/c < 0.8$), transonic ($0.8 < \dot{R}/c < 1.2$), and supersonic ($\dot{R}/c > 1.2$). The time-series of $\dot{R}/c$ in Figure 5 shows that, in the presence of high-frequency amplitude-modulation, the bubble oscillations become more violent. The frequency components of the time series and their amplitudes in the system can be examined by spectral analysis, thereby providing valuable insights into the underlying dynamics of the system. The analysis shows that prominent peaks exist at intervals of

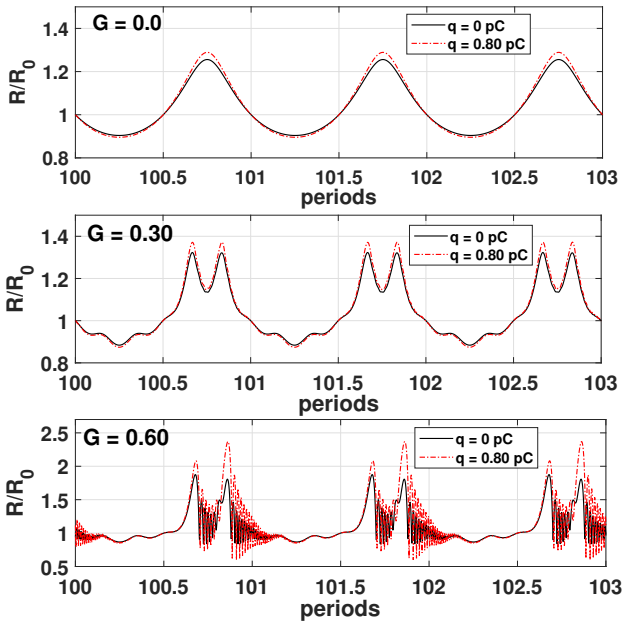

Figure 3: Plot of R/R_0 as a function of driving periods for a neutral bubble (black-thick) and a bubble with charge $q = 0.8$ pC (red-dashed) at different values of G. Other parameters remain unchanged.

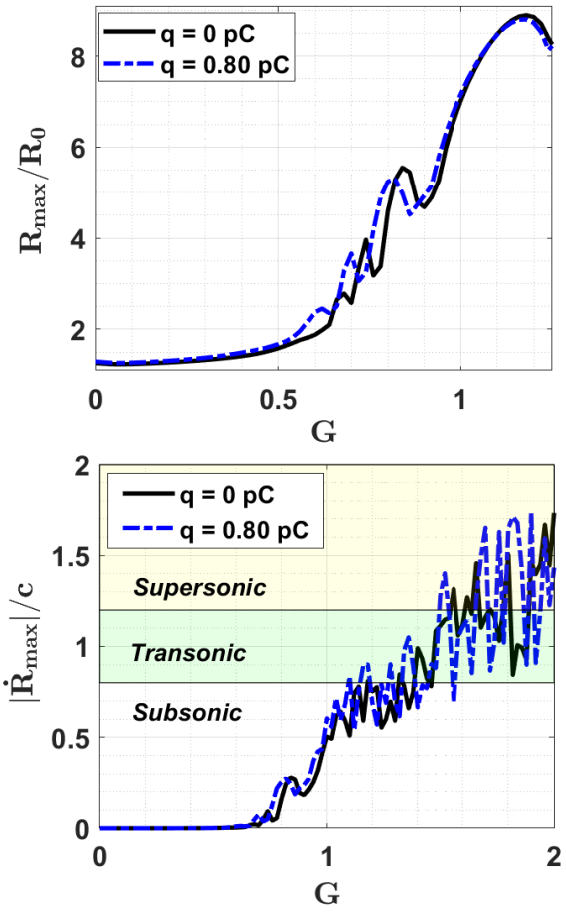

Figure 4: (a) Maximum radius R_{max}/R_0 and (b) Maximum Mach number $|\dot{R}_{max}|/c$ plotted against the modulation amplitude G for a neutral bubble (black-thick) and a bubble with charge $q = 0.8$ pC (blue-dashed). The driving pressure is $P_s = 0.8P_0$ and other parameters remain unchanged.

10,000 Hz which is the fundamental frequency of the source signal – indicating that there is a strong periodic component in the time series. The presence of prominent peaks at regular intervals of 10,000 Hz suggests that the bubble oscillator generates harmonics at multiples of the fundamental frequency.

The effect of the high-frequency amplitude modulation on the bubble velocity can further be understood from Fig. 4(b). The plot in Fig 4(b) shows the maximum Mach number as a function of modulation amplitude G for a neutral and a charged bubble at $q = 0.80$ pC. As G increases from zero to $G = 0.78$ Pa and $G = 0.74$ Pa for the neutral and charged bubbles, respectively, at $q = 0.80$ pC, the bubble velocity increases only slightly, with a maximum Mach number of 0.05 within this range. However, as G rises above $G = 0.78$ Pa and $G = 0.74$ Pa for the neutral and charged bubbles, respectively, at $q = 0.80$ pC, the bubble Mach number increases rapidly for very small changes in the bubble oscillation amplitude. When $G > 1.48$ Pa, the bubble moves beyond the subsonic region into the transonic region. Beyond $G > 1.90$ Pa, the bubble is characterized by supersonic velocities, where its velocity in the medium significantly exceeds the speed of sound c. In general, the introduction of high-frequency amplitude modulation increases the maximum radius of the bubble during the expansion phase. This increased maximum radius causes the bubble to collapse or contract more violently.

Figure 6 plots the $\dot{R}/c$ versus R/R_0 phase portrait for a bubble with charge $q = 0.8$ pC for four different modulation amplitudes, G. As clearly shown, the phase portrait is a regular period-one orbit in the absence of amplitude modulation ($G = 0$ Pa) for the parameters used in the simulation. This corresponds to the time series shown in Fig. 3 (upper panel). Amplification of the orbit, and increased irregularity are manifested as the modulation amplitude G increases, due to the peak shouldering and after-bounces observed in the time series for R/R_0 and $\dot{R}/c$ in Figs. 3 and 5. The Poincaré points coloured red in Fig. 6 indicate that the orbit is a period-one attractor that is stable over a wide range of G values. However, the bubble attractor vibrates with increased velocity and rapidly expanding radius as the modulation amplitude increases beyond a threshold value G_{th}. This is illustrated in the bifurcation diagram (Fig. 7) where a transition point, G_{th} is evident. The dynamics for $G > G_{th}$ is typical of a bursting oscillation, wherein the orbits occasionally visit the quiescent state sandwiching the spikes of the time series, and returns as shown in Figs. 3 and 5 for $G = 0.6$ Pa. This happens because the variables evolve on two distinct time scales [9–12]. In the latter part of this paper, the features of these vibrations, and their dependence on G and the quantity of charge q, will be explored in detail.

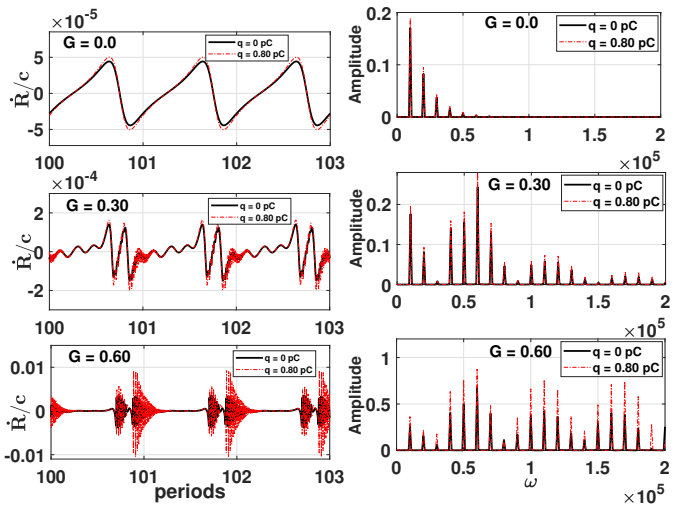

Figure 5: Plot of $\dot{R}/c$ (Mach number) as a function of driving periods and the corresponding spectral analysis for a neutral bubble (black-thick) and a bubble with charge $q = 0.8$ pC (red-dashed) at different values of G. Other parameters remain unchanged. The right-hand side shows the spectral analysis of the corresponding time series.

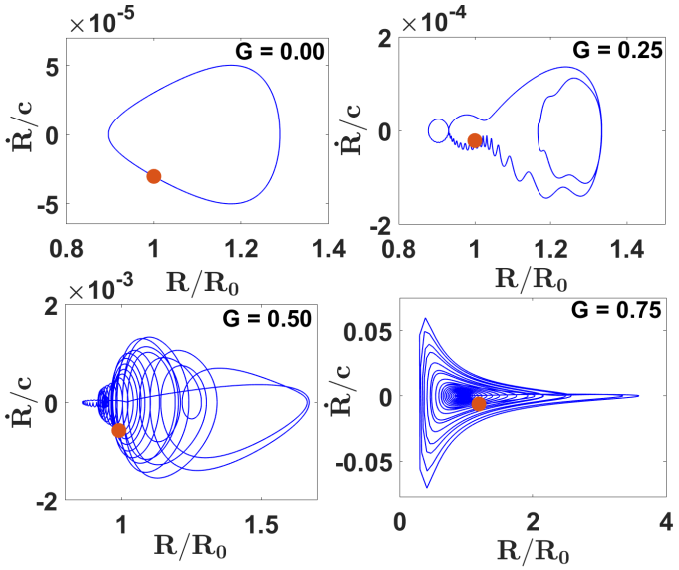

Figure 6: $\dot{R}/c$ versus R/R_0 phase plots and Poincaré map (red points) at different values of the modulation amplitude G for a bubble with charge $q = 0.8$ pC. The driving pressure is $P_s = 0.8P_0$, driving frequency $\nu = 10$ kHz and other parameters remain unchanged.

Notably, for larger values of the pressure amplitude – e.g. $P_s = 2P_0$, the dynamics of the bubble shown in Figs. 6 and 7 is remarkably different for both the neutral ($Q = 0$) and charged ($Q \neq 0$) bubbles. In this case, chaotic dynamics emerges via period-doubling bifurcations from a period-two attractor (when $G = 0$) with increased modulation amplitude, as shown in Fig. 8. The impact of electrostatic charge on the bifurcation structure is clearly evident. First, the size of the attractor shrinks progressively with increasing charge. Secondly, the chaotic dynamics is controlled in certain regimes of G, namely: $G \in [2.29 : 2.41]$, $[3.1 : 3.5]$, $[4.05 : 5.20]$, $[5.70 : 6.07]$. In particular, the window $G = [4.05 : 5.20]$, shows clearly that the control mechanisms are characterised by reversed period-doubling bifurcations. The attractor trajectories and their corresponding Poincaré points for three values of G in the controlled regimes are illustrated in Figs. 9 and 10

Next, we examine the impacts of G on the Blake's threshold, P_{Blake}, which is the pressure threshold above which an acoustically forced bubble expands rapidly, culminating in cavitation. There is a higher threshold after the Blake's threshold known as the transient cavitation threshold, P_{tr}. This is the minimum acoustic pressure required for the bubble to collapse violently after its maximum expansion at near-sound velocities. Essentially, the bubble is in an unstable regime at pressures between the Blake's and transient cavitation thresholds. The maximum Mach Number, $|\dot{R}_{max}|/c$, for $P_s < P_{tr}$, increases as a function of the driving frequency whereas, for $P_s > P_{tr}$, the maximum Mach Number decreases [29]. The expansion-compression ratio $\zeta = (R_{max} - R_0)/(R_0 - R_{min})$ was introduced by Hongray *et al* [28, 29] as a useful dimensionless measure of the relative extent of bubble expansion to compression. Plotting ζ as a function of the driving pressure ratio, P_s/P_0, allows one to locate quickly both Blake's threshold P_{Blake} and the transient cavitation threshold P_{tr}. Figure 11 shows plots of ζ vs P_s/P_0 for a charged bubble with $q = 0.80$ pC in the absence and presence of high-frequency amplitude modulation. Here, as P_s/P_0 increases, the value of ζ rises until it peaks at $P_s = P_{Blake}$ followed by a minimum at $P_s = P_{tr}$. Hongray et al. [29] established the effect of charge and the equilibrium radius R_0 on the ratio ζ in their studies. The effect of high-frequency amplitude modulation on threshold pressures is shown for two different values of the modulation G. Blake's threshold P_{Blake} is $1.085P_0$, $1.1225P_0$, and $1.1325P_0$ for $G = 0, 0.05$, and 0.10 Pa, respectively. Moreover, the transient cavitation threshold, P_{tr}, is at $P_s = 1.1075P_0$, $P_s = 1.1400P_0$, and $P_s = 1.1425P_0$ for $G = 0$ Pa, $G = 0.05$ Pa, and $G = 0.10$ Pa, respectively. Remarkably, an increase in the modulation amplitude G, shifts the threshold pressures to higher P_s values. This could be attributable to high-frequency-induced vibration effects which cause the bubble to expand more rapidly due to decreases in the effective surface tension and damping [28].

Another important threshold for charged bubble dynamics is the maximum charge q_h that a bubble can carry. Beyond q_h, the bubble model's minimum radius R_{min} may become less than that corresponding to the van der Waals hard core radii h for the gas contained within the bubble. Previous research has established the effect of driving pressure P_s and equilibrium radius R_0 on q_h [28, 29]. Figure 12 shows a plot of q_h as a function of the modulation amplitude G for a bubble of equilibrium radius $R_0 = 5$ μm with different driving frequencies. Clearly, the value of the

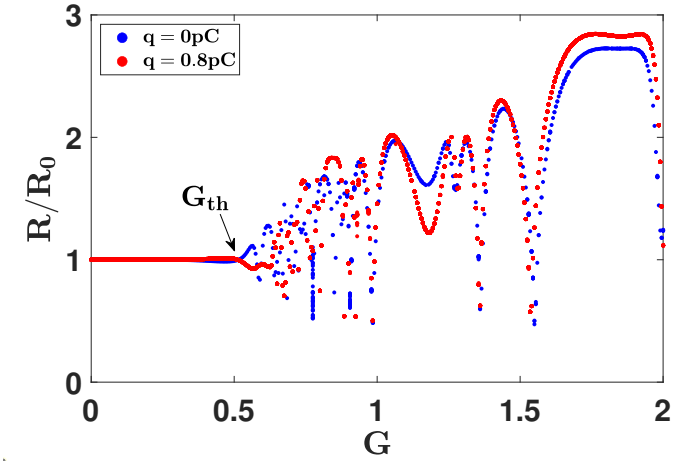

Figure 7: Bifurcation diagram of R/R_0 varying with the modulation amplitude G for bubble charges $q = 0$ pC (blue dots) and $q = 0.8$ pC (red dots). G_{th} is the transition point indicating the onset of bubble vibration. The driving pressure is $P_s = 0.8P_0$, driving frequency $\nu = 10$ kHz and other parameters remain unchanged.

threshold q_h decreases significantly as the high-frequency modulation amplitude G increases from zero. Similarly, q_h decreases with increasing driving frequency of the acoustic pressure field from $G = 0$ Pa to $G = 0.70$ Pa. The bubble's ultrasonic cavitation threshold decreases significantly in the presence of electrostatic charges due to a decrease in effective surface tension. Furthermore, the high-frequency amplitude-modulation serves to reduce the magnitude of the effective surface tension even further. The decrease in the value of the threshold q_h due to high-frequency amplitude-modulation can be explained in relation to the reduction of the bubble wall resistance to rupture due to decreased surface tension [57]. Remarkably, the curve has a plateau-like feature beyond $G = 0.70$ Pa, wherein increased modulation amplitude does not impact on the value of q_h regardless of the driving frequency of the acoustic pressure field. This demonstrates that for $G > 0.70$ Pa, the effect of vibration due to cooperation between the frequencies of the driving acoustic field (ω) and the modulating force (Ω) on the maximum allowed bubble charge eventually saturates for $R_0 = 5$ μm. The minimum q_h for the equilibrium bubble radius $R_0 = 5$ μm was estimated to be 1.24 pC. The area above the curve in Figure 12, which is dependent on the linear frequency ν is physically unreachable for the bubble because the minimum radius becomes less than that corresponding to the van der Waals hard core radii $R_{min} > h$ of the enclosed gas atoms.

3.2. Effect of charge on the vibrational resonance of the bubble

We start by focusing on the effect of charge variation on the bubble's response to dual-frequency-driven acoustic fields. We computed the quantity Q/Q_{unc}, where Q_{unc} is the response amplitude of the uncharged bubble (i.e. for $q = 0$). The dependence of the response amplitude ratio Q/Q_{unc} on the charge q is illustrated in Figure 13 for different values of modulation amplitude G with a driving pressure $P_s = 0.8P_0$, bubble equilibrium radius $R_0 = 5.0$ μm and other parameters remain as previously stated. The response amplitude for the uncharged bubble is represented by Q_{unc} ($q = 0$ pC). In Figure 13, the ratio Q/Q_{unc} has a value of unity when $q = 0$ pC and the response amplitude is either amplified ($Q/Q_{unc} > 1$) or attenuated ($Q/Q_{unc} < 1$) as charge increases from $q = 0$ pC. A close look at Figure 13 shows that there is an amplification of the response amplitude as charge increases for G lying between 0.25 Pa $\leq G \leq$ 0.70 Pa. For $G = 0.60$ and $G = 0.70$, the response amplitude is significantly amplified to about 1.45 and 1.72 times the input signal, respectively. However, for $G > 0.70$ Pa and especially between $G = 0.72$ Pa and 1.0 Pa, the response amplitude initially underwent a marked attenuation until around $q = 0.55$ pC, after which the response amplitude increases as the bubble charge increases further. The attenuation, characterized by the inversion of the VR curve, corresponds only to a ~20% reduction in the value compared to the uncharged case since Q/Q_{unc} ~0.8 at the inversion. For $G \geq 1.00$ Pa the effect of charge on the response am-

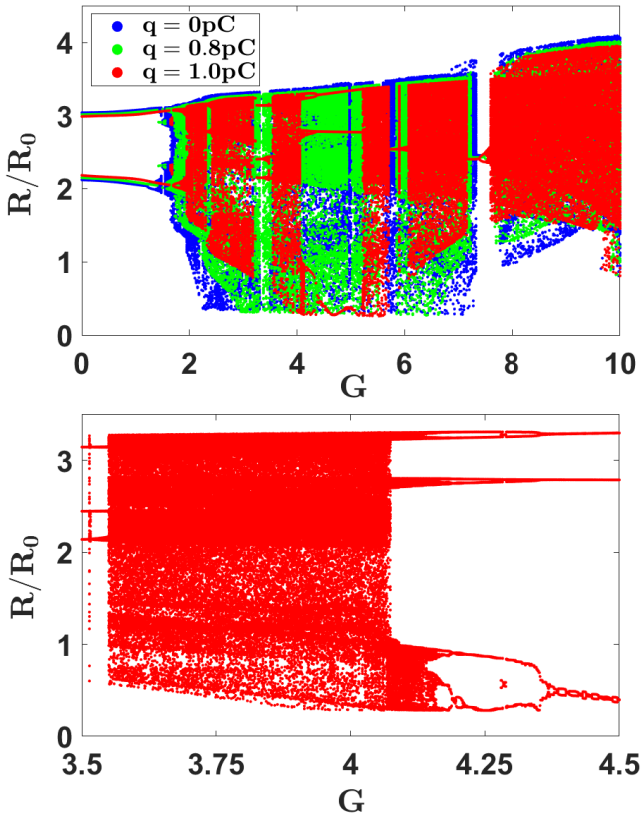

Figure 8: Bifurcation diagram of R/R_0 varying with the modulation amplitude G for bubble charges $q = 0$ pC (blue dots), $q = 0.8$ pC (green dots) and $q = 1.0$ pC (red dots). The bottom plot is the zoom of the periodic window where reversed period-doubling bifurcation appeared. The driving pressure is $P_s = 2.0P_0$, driving frequency ν = 500 kHz and other parameters remain unchanged.

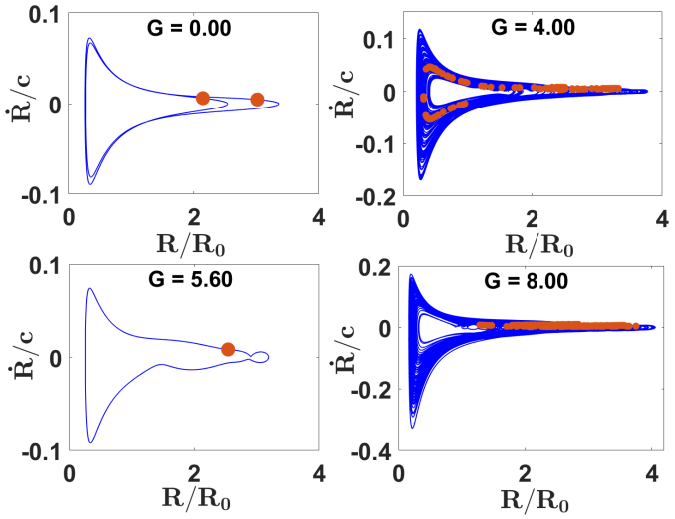

Figure 9: $\dot{R}/c$ versus R/R_0 phase plots and Poincaré map (red points) at different values of the modulation amplitude G for a bubble with charge $q = 0.8$ pC. The driving pressure is $P_s = 2.0P_0$, driving frequency $\nu = 500$ kHz and other parameters remain unchanged.

plitude of the bubble eventually saturates, and variations in the bubble charge produce no significant changes in the response amplitude. Thus, the effect of the high-frequency amplitude-modulation eventually compensates for the electrostatic effect caused by the charge.

In Figures 14(a) and (b), the response amplitude Q is plotted against the modulation amplitude G and acoustic driving frequency ω for different values of the charge q . It is characterized by multiple resonance peaks and decreases slightly as the bubble charge increases for $0 < G < 1.0$ Pa. However, as the charge increases further, the resonance peaks appear at lower values of the modulation amplitude G. The resonance peaks for $q = 0$ pC are at $G = 0.68$ Pa, 0.74 Pa, and 0.85 Pa. The $q = 0.50$ pC resonance peaks are slightly shifted to lower G values at $G = 0.66$ Pa, 0.72 Pa, and 0.83 Pa. Furthermore, for $q = 1.00$ pC, there are now only two distinct resonance peaks at $G = 0.68$ Pa and 0.81 Pa. Thus, the vibrational effect is characterized by multiple vibrational resonance peaks. The amplification of the input signal at the highest resonance peak is by factors of 7.26, 6.82, and 5.72 at bubble charge values of $q = 0$ pC, $q = 0.50$ pC, and $q = 1.00$ pC, respectively. Figure 14(b) shows that the bubble's resonance amplitude is directly proportional to the driving frequency ω of the acoustic field and the quantity of charge, with distinct resonance peaks. The response amplitude does not change significantly as the driving frequency increases from zero to around 60 kHz. However, there are about four distinct resonance peaks between $60 - 150$ kHz, specifically at $\omega = 63.46$ kHz, 76.02 kHz, 93.62 kHz, and 122.52 kHz for a bubble with charge $q = 1.00$ pC. The resonance peaks occur at lower values of the acoustic driving frequency as the bubble charge increases.

It is also worth noting that, in contrast to previous

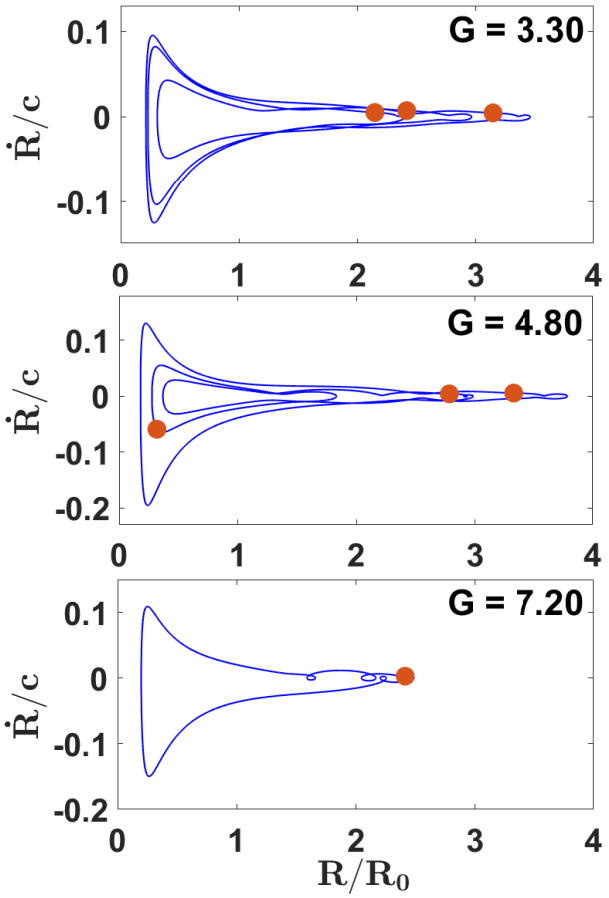

Figure 10: $\dot{R}/c$ versus R/R_0 phase plots and Poincaré map (red points) at different values of the modulation amplitude G for a bubble with charge $q = 1.0$ pC. The driving pressure is $P_s = 2.0P_0$, driving frequency $\nu = 500$ kHz and other parameters remain unchanged.

cases of VR, the VR response curves in this case exhibit resonance at relatively low values of the introduced high-frequency modulation amplitude G compared to the acoustic driving pressure $P_s \sim 10^5$ Pa.

3.3. Effect of driving pressure on the vibrational resonance of the bubble

Previous research has shown that the driving pressure $P_s = \kappa P_0$ exerts a significant effect on the dynamics of acoustically driven bubbles. We now examine the dependence of VR on the driving pressure P_s of the acoustic field (Figure 15). The pressure thresholds for a 5 μm bubble are: Blake's threshold, $P_{Blake} = 1.085P_0$; and the transient cavitation threshold, $P_{tr} = 1.108P_0$. The dependence of the response amplitude Q on the modulation amplitude G at four different driving pressures is shown in Figure 15(a). The values used were $P_s = 0.9P_0$ (i.e. below Blake's threshold), $P_s = 1.085P_0$ (at Blake's threshold), $P_s = 1.1P_0$ (between the Blake and transient cavitation thresholds) and $P_s = 1.2P_0$ (beyond the transient cavitation threshold). As already indicated the bubble is in an unstable regime for driving pressures between the Blake's and transient cavitation thresholds. Furthermore, after

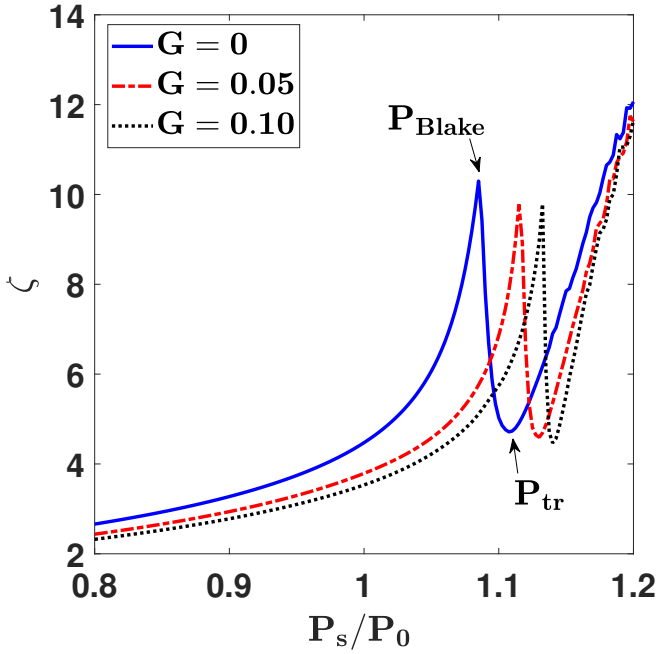

Figure 11: Plot of ζ (expansion-contraction ratio) as a function of the driving pressure ratio P_s/P_0 at $\nu = 10$ kHz and $R_0 = 5$ μm at; (a)$G = 0$ Pa showing the locations of the Blake's threshold pressure P_{Blake} and the upper transient threshold pressure P_{tr}. (b) $G = 0$ Pa (blue-thick), $G = 0.05$ Pa (red-dashed) and $G = 0.10$ Pa (black-dotted).

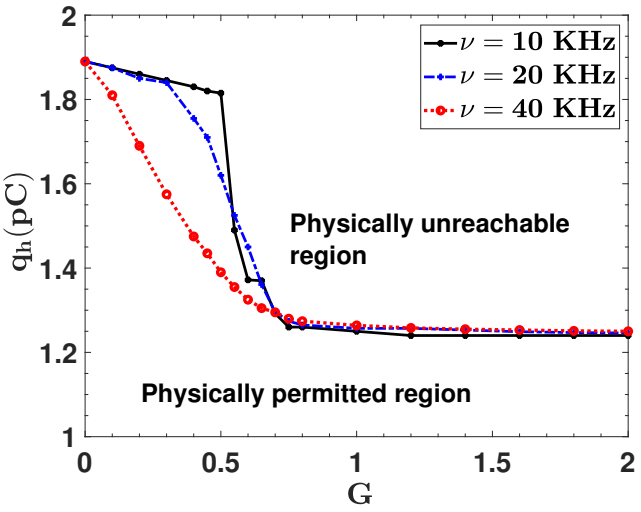

Figure 12: Plot of q_h as a function of the modulation amplitude G for a bubble of equilibrium radius $R_0 = 5$ μm at driving frequencies $\nu = 10$ kHz (black-thick), $\nu = 20$ kHz (blue-dashed) and $\nu = 40$ kHz (red-dotted). The driving pressure is $P_s = 0.8P_0$ and other parameters remain unchanged. The area below each curve corresponds to the physically permitted region for the bubble. The area above each curve is the physically unreachable region for the bubble.

maximal radial expansion, the bubble collapses violently above the transient cavitation threshold. At driving pressures below Blake's threshold, the bubble is at its most stable. This is illustrated in Figure 15(a), where the response amplitude is more pronounced for $P_s = 0.9P_0$, with three resonance peaks at $G = 0.62$ Pa, 1.06 Pa, and 3.54 Pa. For this case, the amplification due to VR at the highest resonance peak ($G = 3.54$ Pa) is by a factor of 45.24 of the amplitude at $G = 0$ Pa. However, for the other driving pressure values used in Figure 15(a), there exist single resonance peaks located at $G = 2.34$ Pa, $G = 2.40$ Pa, and 2.64 Pa for $P_s = 1.085P_0$, $P_s = 1.1P_0$, and $P_s = 1.2P_0$, respectively. The amplification of the input signal due to VR at these resonance peaks is 16.51, 10.18, and 2.81 for $P_s = 1.085P_0$, $P_s = 1.1P_0$, and $P_s = 1.2P_0$, respectively. When the driving pressures exceed Blake's threshold, the resonance peaks shift slightly to higher modulation amplitude G values with decrease in the amplification of the input signal due to VR. The rough nature of the response curve that appears as the modulation amplitude G increases for driving pressures above Blake's threshold is a further signature of the bubble dynamics' instability in this case. The instability in the response curves for pressures above the Blake's threshold can be better understood by referring to Figure 15(b). For increasing values of the modulation amplitude G ($0 - 2.00$ Pa), the response amplitude of the bubble is plotted as a function of the driving pressure ratio Ps/P_0 in Figure 15(b). In the absence of the high-frequency modulation ($G = 0$ Pa), the bubble does not vibrate. Thus, no resonance peaks exist at any driving pressure. However, when the modulation is switched on, the bubble vibrates with multiple peaks and the number of resonance peaks increases as the value of G increases. In general, as the value of G increases, the response amplitude due to the pulsation effect caused by the increased effective pressure on the bubble also increases. In the presence of a driving pressure above Blake's threshold, the pulsation effect becomes more pronounced as the modulation amplitude of the high-frequency force increases.

3.4. Effect of equilibrium radius on the vibrational resonance of the bubble

Figures 16 and 17 show the dependence of the acoustically driven bubble's response amplitude Q on the ambient or equilibrium bubble radius, R_0. This is of interest because the compressibility function $\lambda = -R_0/c$ is related to R_0 [2, 58]. Figure 16(a) shows the response amplitude Q as a function of the equilibrium bubble radius R_0 at four different modulation amplitudes G. The equilibrium radius is directly proportional to the resonance amplitude of the acoustically-driven bubble, as shown in Figure 16(a), and the system is enhanced and maximizes as the equilibrium radius increases. VR, characterized by the multiple peaks in the resonance curves, occurs at several values of R_0, ranging from 1.5 μm to 10.0 μm. For $R_0 > 8$ μm, a random-walk-like pattern appears in the $Q - R_0$ resonance curve, indicating the onset of aperiodicity in the bubble oscillation for modulation amplitudes greater than 0.5 Pa. The most dominant VR peaks appears within the stable and periodic oscillation window when R_0 is 9.1 μm, 6.9 μm, 7.9 μm, and 6.8 μm for $G = 0.50$ Pa, 0.75 Pa, 1.00 Pa, and

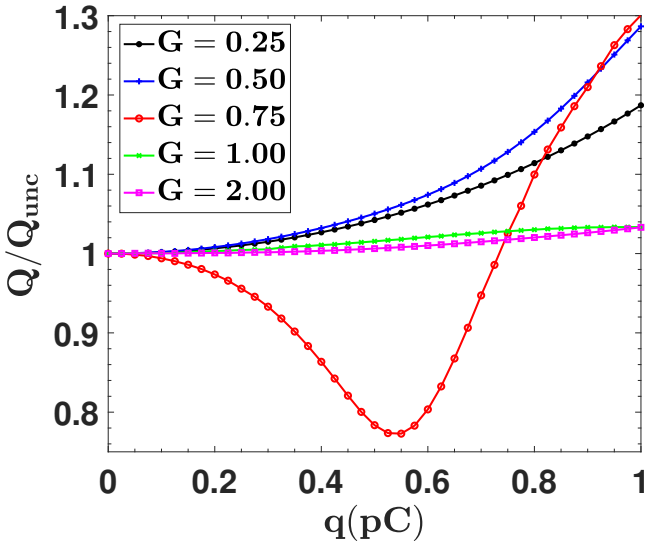

Figure 13: Effect of G on the response amplitude ratio Q/Q_{unc} of the charged-bubble. Q_{unc} represents the response amplitude for the uncharged bubble (q = 0 pC). Q/Q_{unc} has a value of unity when q = 0 pC, it either amplifies ($Q/Q_{unc} > 1$) or de-amplifies ($Q/Q_{unc} < 1$) as the quantity of charge increases. Between G = 0.7 Pa and G = 1.0 Pa, there appears an inversion of the response amplitude.

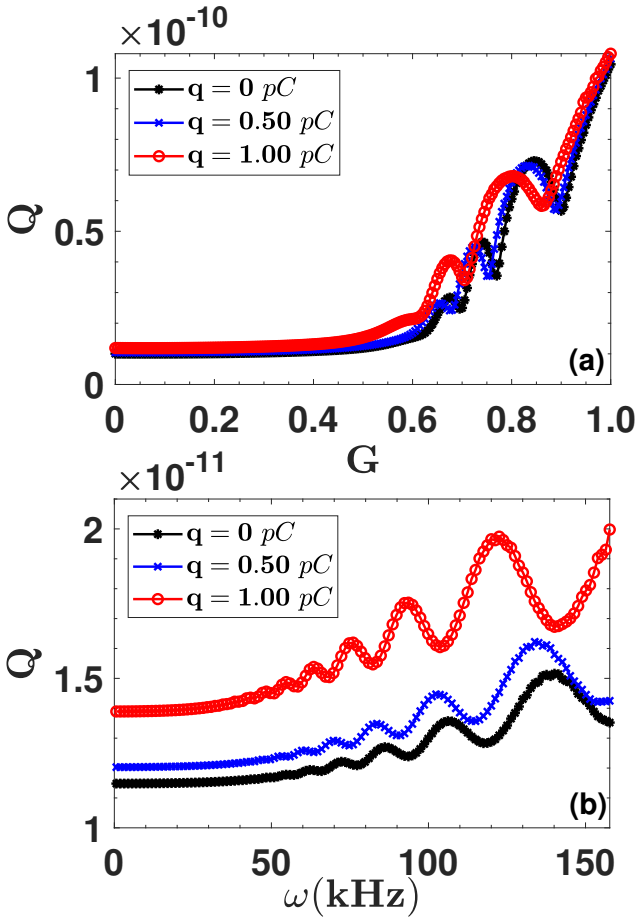

Figure 14: Plot of response amplitude Q against (a) modulation amplitude G (b) driving frequency ω at G = 0.50 Pa for different values of bubble charge (q = 0 pC, q = 0.50 pC, q = 1.00 pC). The driving pressure is $P_s = 0.8P_0$ and other parameters remain unchanged.

2.00 Pa, respectively. The amplification of the input signal due to VR at these resonance peaks is by factors of 20.61, 36.43, 60.00, and 4.47 for G = 0.50 Pa, 0.75 Pa, 1.00 Pa, and 2.00 Pa, respectively. By increasing the driving frequency ω with fixed bubble ambient radius R_0, the system's response amplitude can be enhanced. Figure 16(b) shows a plot of the response amplitude Q as a function of the acoustic driving frequency ω for different bubble equilibrium radii R_0 = 4.0 μm, 5.0 μm, and 6.0 μm. Again, we found multiple peaks for all values of R_0, with significant enhancement of Q as the equilibrium radius becomes larger. The most dominant VR peaks within the frequency range investigated for R_0 = 4.0 μm were at 135.09 kHz and 175.56 kHz. Within the window for stable and periodic oscillations at R_0 = 5.0 μm, the most dominant VR peaks were at 102.42 kHz and 133.83 kHz, with an aperiodic window within the frequency range 170 − 200 kHz. In the frequency range 135 − 170 kHz, the aperiodic window was observed for a large bubble of radius R_0 = 6.0 μm. The dominant VR peaks are located at 82.31 kHz and 106.19 kHz.

Figure 17 plots the dependence of the response amplitude Q on the modulation amplitude G for bubble equilibrium radii R_0 = 4.0 μm, 5.0 μm, and 6.0 μm. The response curve in the range G = 0 − 6.00 Pa is shown in two plots: Figure 17(a) (G = 0 − 2.34 Pa) and Figure 17(b) (G = 2.34 - 6.00 Pa). At lower values of the modulation amplitude G, the variations in response amplitude with changes in the bubble ambient radius are more pronounced. As previously stated, the pulsation effect caused by increased effective pressure on the bubble accounts for the roughness of the response curve at higher G values. For the bubble equilibrium radii of R_0 = 4.0 μm, 5.0 μm and 6.0 μm used, there are five distinct resonance peaks within the range G = 0 − 6.00 Pa. Those for R_0 = 4.0 μm are at G = 0.92 Pa, 1.20, 1.56 Pa, 2.22 Pa, and 4.68 Pa, corresponding to input signal enhancement factors of 8.00, 14.29, 23.76, 38.84, and 68.19, respectively. The resonance peaks for R_0 = 5.0 μm occur at G = 0.72 Pa, 0.82 Pa, 1.18 Pa, 1.86 Pa, and 4.38 Pa, corresponding to input signal enhancement factors of 4.27, 6.76, 13.32, 26.14, and 54.43, respectively. Furthermore, the resonance peaks for R_0 = 6.0 μm are located at G = 0.60 Pa, 0.70 Pa, 0.88 Pa, 1.56 Pa, and 4.44 Pa, corresponding to input signal enhancement factors of 2.23, 4.43, 7.92, 18.11, and 44.40, respectively. In general, the values of G at which the VR peaks occur shift to lower values as the equilibrium radius of the bubble increases. Furthermore, as the equilibrium radius increases, the amplification effect of the input signal decreases. Consequently, the smaller the equilibrium radius, the greater the effect of signal amplification due to VR.

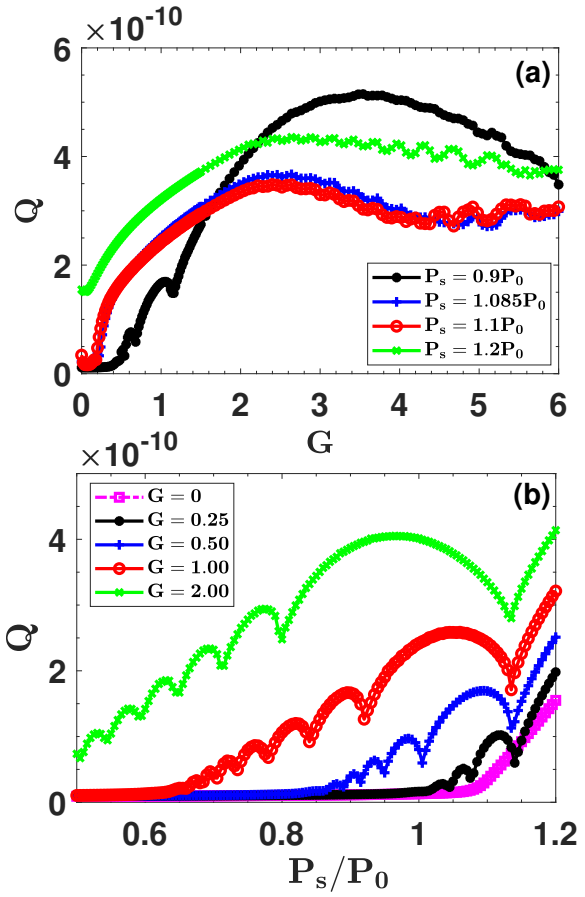

Figure 15: Plot of response amplitude Q against (a) modulation amplitude G for a bubble with charge $q = 0.50$ pC for different values of bubble driving pressure ($P_s = 0.9P_0$, $P_s = 1.085P_0$, $P_s = 1.1P_0$, $P_s = 1.2P_0$). (b) driving pressure ratio P_s/P_0 for a bubble with charge $q = 0.50$ pC at $G = 0$ Pa, 0.25 Pa, 0.50 Pa, 1.00 Pa, 2.00 Pa. Other parameters remain unchanged.

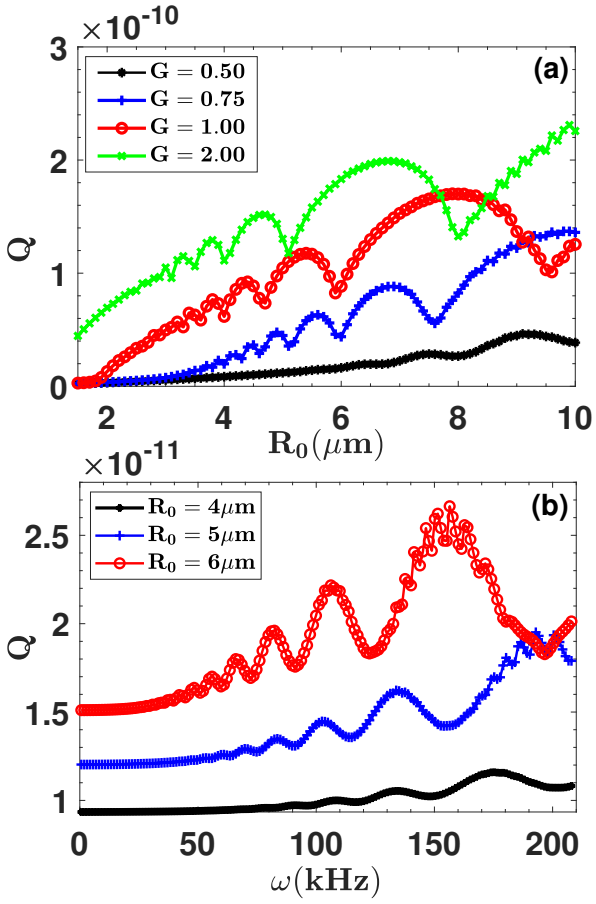

Figure 16: Plot of response amplitude Q against (a) equilibrium radius R_0 for a bubble with charge $q = 0.50$ pC at $G = 0.50$, 0.75, 1.00, 2.00. (b) driving frequency ω at $G = 0.50$ for different values of the equilibrium radius ($R_0 = 4$ μm, $R_0 = 5$ μm, $R_0 = 6$ μm). The driving pressure is $P_s = 0.8P_0$ and other parameters remain unchanged.

3.5. Effect of surface tension on the vibrational resonance of the bubble

We demonstrated above that VR can be induced by varying the quantity of charge on the bubble, or its equilibrium radius, or the parameters of the acoustic driving field $P_s \sin \omega t$, or the modulating high-frequency amplitude G. We now investigate the effect of the liquid properties and, in particular, the surface tension on the occurrence of the VR phenomenon. It is of note that the surface tension of a liquid can be altered slightly by using surfactants such as ethoxylated octylphenol (Photoflo®), 4-(1,1,3,3-Tetramethylbutyl)phenyl-polyethylene glycol (Triton® X-100), polyoxyalkylene alkyl ether (NCW®-1002) and other compounds due to their adsorption at solid/liquid and gas/liquid interface [59–61]. This could be of significance in relation to the technological applications of bubbles. Thus, investigating surface tension effects will illuminate the likely impact of surfactants on VR. This is illustrated in Figure 18(a) where we present a plot of the response amplitude Q as a function of surface tension σ at various modulation amplitudes G. The response amplitude is evidently inversely proportional to the surface tension. Furthermore, as the value of G increases, the relationship between Q and σ becomes nonlinear. Figure 18(b) plots the response amplitude Q versus the acoustic driving frequency ω for different values of surface tension σ ($\sigma = 0.06$, $\sigma = 0.0725$, $\sigma = 0.08$). The surface tension values were chosen to be close to the standard value of 0.0725 Nm^{-1} for water at room temperature. Remarkably, increasing the driving frequency ω at a specific surface tension σ increases the system's response amplitude. Here, an aperiodic window for $\omega > 160$ kHz in the frequency range investigated, characterized by a random-walk-like pattern can be observed in the response curve. The most dominant resonance peaks within the stable and periodic oscillation window are at 96.76 kHz, 126.92 kHz for $\sigma = 0.06$ Nm^{-1}; 102.42 kHz, 133.83 kHz for $\sigma = 0.0725$ Nm^{-1} and 106.81 kHz, 140.74 kHz for $\sigma = 0.08$ Nm^{-1}. As the surface tension increases, the VR resonance peaks shift slightly to higher values of the modulation amplitude G.

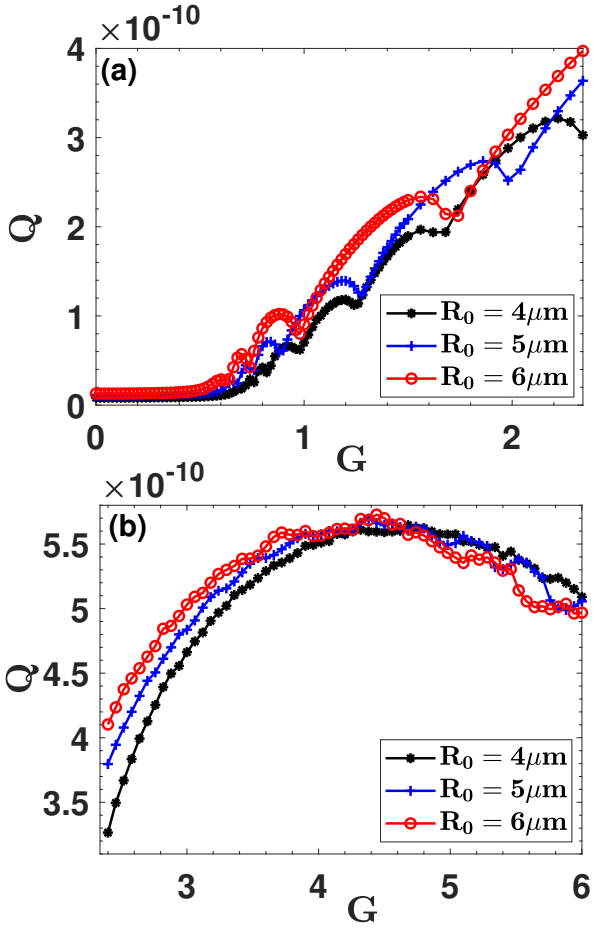

Figure 17: Plot of response amplitude Q against modulation amplitude G for a bubble with charge $q = 0.50$ pC for different values of the equilibrium radius ($R_0 = 4$ μm, $R_0 = 5$ μm, $R_0 = 6$ μm): (a) $G = 0$ - 2.34 pa, 5.0 Pa and (b) $G = 2.34$ - 6.00 Pa. The driving pressure is $P_s = 0.8P_0$ and other parameters remain unchanged. The bubble size impacts on Q more significantly at weak G values.

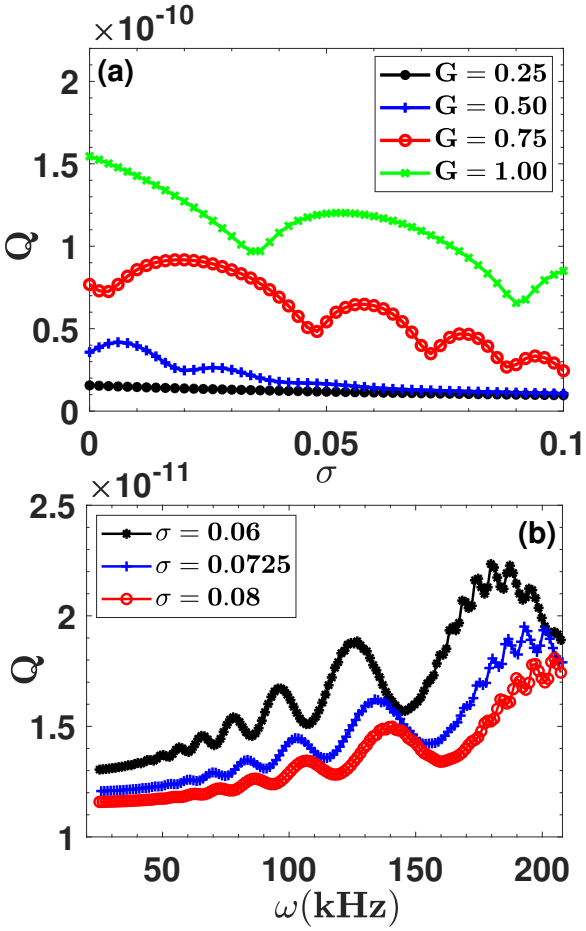

Figure 18: Plot of response amplitude Q against (a) surface tension σ for a bubble with charge $q = 0.50$ pC at $G = 0.50$ Pa, 0.75 Pa, 1.00 Pa, 2.00 Pa showing inverse relationship between Q and σ, with signal enhancement promoted by increase in the modulation. (b) Q vs driving frequency ω at $G = 0.50$ Pa for different values of the surface tension ($\sigma = 0.06$ Nm^{-1}, $\sigma = 0.0725$ Nm^{-1}, $\sigma = 0.08$ Nm^{-1}) showing increased response with increase in ω as well as the appearance of aperiodic window at higher values of ω. The driving pressure is $P_s = 0.8P_0$ and other parameters remain unchanged.

4. Conclusions

We have investigated the dynamics of a charged bubble moving in a compressible liquid while being driven by amplitude-modulated acoustic waves. We focused closely on the possible impacts of the electrostatic charges and modulation on the dynamical properties of the bubbles, such as the Mach number, bifurcations, phase space trajectories and attractors in the Poincaré section – all of which were not considered in recent papers by some of us [8, 14]. Consideration of the liquid's compressibility is essential when dealing with cases where large-amplitude oscillations are encountered – such as are often found in biomedical applications.

Our investigation of the dynamics and the occurrence of VR in a charged bubble oscillator driven by an high-frequency amplitude-modulated acoustic pressure field has led to several significant conclusions. Our charged oscillator model largely preserves the higher-order nonlinearities, which are essential for capturing the complete dynamics. By dropping these higher-order damping terms for the unforced oscillator case, we recovered the expressions for the linear natural frequency and the linear oscillator damping obtained earlier by Hongray *et al.* [28]. The potential structure of the charged bubble has been established, and the stability analysis of its equilibrium states reveals the existence of one, two, three or no equilibrium states, depending on the value of the electrostatic charge it carries. Notably, the existence of the three equilibria state could not have been established by Grigor'ev and Zharov [52] because their stability analysis was based on the linear model.

High-frequency amplitude-modulation increases the amplitude of the bubble oscillation, with the time-series exhibiting peak-shouldering and, at the same time, shock waves can arise. Remarkably, a certain pressure amplitude – viz. $P_s = 2P_0$ – can drive the bubble into chaotic

states via period-doubling bifurcations. However, progressive increase in the charge can counter this chaos-induced effect by controlling its appearance in some windows of the modulation amplitudes through multiple reversed period-doubling bifurcation sequences. The charge-facilitated chaos control arising from the cooperation between electrostatic charges and the modulation amplitude was not reported by Hongray *et al.* [29] in their study, wherein it was found that charge always advance the period-doubling bifurcations. In addition, we also found that the bubble Mach number grows quickly with small increase in the modulation amplitude beyond $G = 0.78$ Pa and $G = 0.74$ Pa for the neutral and charged bubbles, respectively. The bubble enters the transonic dynamics zone when $G > 1.48$ Pa, and the supersonic zone when $G > 1.90$ Pa. As the modulation amplitude rises, Blake's threshold and the transient cavitation threshold both shift to higher values of the pressure amplitude P_s/P_0 reported by Hongray *et al.* [28], perhaps attributable to the greater bubble expansion due to a reduction in the effective surface tension and damping. With stronger high-frequency amplitude-modulation, the bubble maximal charge threshold decreases considerably. Because surface tension is reduced by high-frequency modulation, the bubble's resistance to rupture in the presence of electrostatic charges is reduced, thus lowering both thresholds.

For $G > 1.00$ Pa, the charge's impact on the bubble's VR is negligible because the effect of the high-frequency modulation balances out the electrostatic effects. No resonance peak with driving pressure was found in the absence of high-frequency modulation ($G = 0$ Pa); but with rising G, multiple VR peaks appeared due to the pulsation effect arising from increased effective pressure on the bubble. The resonance amplitude of the acoustically-driven bubble increases proportionally with the equilibrium radius and, as the equilibrium radius grows, so also do the amplification and enhancement of the system's response. The system's response amplitude increases as the driving frequency ω is raised at fixed bubble equilibrium radius. Increasing the liquid's surface tension results in an increase in the VR signal amplification in direct proportion to the liquid surface tension. Raising the driving frequency ω at fixed surface tension increases the system's response amplitude.

These results promise to stimulate further theoretical and experimental investigations. They relate especially to the understanding and exploration of the practical applications of electrically charged particles for the production of electroaerosols and agarose gel solid–liquid electrolyte [62, 63]. They will also help in in elucidating the possible roles of modulated ultrasound over a charged surface in the generation of single- and multi-electron bubbles in liquid helium [64].

Acknowledgements

The work was supported by the Redeemer's University Research Grant and Staff Development Committee under Grant No. URG&SDC/31/4/250.

Appendix 1 - The charged bubble equation

In the formulation of the charged bubble equation, it was assumed that the bubble underwent only radial oscillations. Thus, the bubble radius R, was expressed in terms of its expansion or contraction variable x taken to be dimensionless. So that $R = R_0(1+x)$ and by substituting it into the charged bubble equation for the case where $G = 0$ Pa (in the absence of the high-frequency modulation), Eq. (3) then becomes

$$\begin{aligned}
&(1+\lambda\dot{x})\,R_0^2\,(1+x)\,\ddot{x} + \frac{4\eta}{c\rho}R_0\ddot{x} = \frac{\delta_1}{\rho}\,(1+x)^{-3\Gamma} \\
&(1-\lambda(1-3\Gamma)\dot{x}) - \frac{R_0^2}{2}\dot{x}^2\,(3+\lambda\dot{x}) - \frac{2\sigma}{\rho R_0(1+x)} \\
&+ \frac{q^2}{8\pi\rho\epsilon R_0^4(1+x)^4}\,(1+3\lambda\dot{x}) - \frac{4\eta\dot{x}}{\rho(1+x)} \\
&\qquad - \frac{\delta_2}{\rho}\,(1-\lambda\dot{x}) + \frac{P_s\lambda\omega}{\rho}\,(1+x)\cos\omega t \quad (13)
\end{aligned}$$

where

$$\begin{aligned}
\lambda = -\frac{R_0}{c}, \qquad \delta_1 = P_0 - P_v + \frac{2\sigma}{R_0} - \frac{q^2}{8\pi\epsilon R_0^4}, \\
\delta_2 = P_0 - P_v + P_s\sin\omega t \quad (14)
\end{aligned}$$

Using $(1+x)^{-3\Gamma} \approx 1 - 3\Gamma x$, and dividing through by $R_0^2(1+x)$, Eq. (13) becomes

$$\begin{aligned}
&(1+\lambda\dot{x})\,\ddot{x} + \frac{4\eta}{\rho c}\frac{\ddot{x}}{R_0(1+x)} = \frac{\delta_1}{\rho R_0^2}\frac{1-3\Gamma x}{(1+x)} \\
&(1-\lambda(1-3\Gamma)\dot{x}) - \frac{3\dot{x}^2}{2(1+x)} - \frac{\lambda\dot{x}^2}{2(1+x)} \\
&- \frac{2\sigma}{\rho R_0^3(1+x)^2} + \frac{q^2}{8\pi\rho\epsilon R_0^6(1+x)^5}\,(1+3\lambda\dot{x}) \\
&- \frac{4\eta\dot{x}}{\rho R_0^2(1+x)^2} - \frac{\delta_2}{\rho R_0^2(1+x)}\,(1-\lambda\dot{x}) \\
&\qquad + \frac{P_s\lambda\omega}{\rho R_0^2}\cos\omega t. \quad (15)
\end{aligned}$$

Using the binomial expansion for the terms $(1+x)^{-n}$, retaining terms up to the quadratic term in x, Eq. (15), after some algebraic manipulation, can be written as

$$\ddot{x}\left[1+\lambda\dot{x}+\frac{4\eta}{\rho R_0 c}(1-x+x^2)\right]+\frac{\delta_1}{\rho R_0^2}\left[-1+(1+3\Gamma)x-(1+3\Gamma)x^2+3\Gamma x^3\right]+\frac{\delta_1\lambda}{\rho R_0^2}(1-3\Gamma)\dot{x}\left[1-(1+3\Gamma)x+(1+3\Gamma)x^2-3\Gamma x^3\right]+\frac{3}{2}\dot{x}^2(1-x+x^2)+\frac{\lambda}{2}\dot{x}^3(1-x+x^2)+\frac{q^2}{8\pi\rho\epsilon R_0^6}(-1+5x-15x^2)+\frac{3q^2\lambda}{8\pi\rho\epsilon R_0^6}\dot{x}(-1+5x-15x^2)+\frac{2\sigma}{\rho R_0^3}(1-2x+3x^2)+\frac{4\eta}{\rho R_0^2}\dot{x}(1-2x+3x^2)+\frac{\delta_2}{\rho R_0^2}(1-x+x^2)+\frac{\delta_2\lambda}{\rho R_0^2}\dot{x}(-1+x-x^2)=\frac{P_s\lambda\omega}{\rho R_0^2}\cos\omega t. \quad (16)$$

It is assumed that the bubble oscillates about its equilibrium radius R_0. This assumption leads to the following approximation

$$\phi=1+\lambda\dot{x}+\frac{4\eta}{\rho R_0 c}(1-x+x^2)\approx 1+\frac{4\eta}{\rho R_0 c},$$

which is valid considering the stability properties that have been established in previous studies [8, 65–67]. Thus, Eq. (16) becomes

$$\ddot{x}+\frac{\dot{x}}{\phi}\left[\left(\frac{\delta_1\lambda}{\rho R_0^2}(1-3\Gamma)-\frac{3q^2\lambda}{8\pi\epsilon\rho R_0^6}+\frac{4\eta}{\rho R_0^2}-\frac{\delta_2\lambda}{\rho R_0^2}\right)x+\left(-\frac{\delta_1\lambda}{\rho R_0^2}(1-9\Gamma^2)+\frac{15q^2\lambda}{8\pi\epsilon\rho R_0^6}-\frac{8\eta}{\rho R_0^2}+\frac{\delta_2\lambda}{\rho R_0^2}\right)x+\left(\frac{\delta_1\lambda}{\rho R_0^2}(1-9\Gamma^2)-\frac{45q^2\lambda}{8\pi\epsilon\rho R_0^6}+\frac{12\eta}{\rho R_0^2}-\frac{\delta_2\lambda}{\rho R_0^2}\right)x^2-\frac{3\Gamma\delta_1\lambda}{\rho R_0^2}(1-3\Gamma)x^3\right]+\frac{3}{2\phi}\dot{x}^2(1-x+x^2)+\frac{\lambda}{2\phi}\dot{x}^3(1-x+x^2)+\frac{1}{\phi}\left(-\frac{\delta_1}{\rho R_0^2}-\frac{q^2}{8\pi\epsilon\rho R_0^6}+\frac{2\sigma}{\rho R_0^3}+\frac{\delta_2}{\rho R_0^2}\right)+\frac{1}{\phi}\left(\frac{\delta_1}{\rho R_0^2}(1+3\Gamma)+\frac{5q^2}{8\pi\epsilon\rho R_0^6}-\frac{4\sigma}{\rho R_0^3}-\frac{\delta_2}{\rho R_0^2}\right)x+\frac{1}{\phi}\left(-\frac{\delta_1}{\rho R_0^2}(1+3\Gamma)-\frac{15q^2}{8\pi\epsilon\rho R_0^6}+\frac{6\sigma}{\rho R_0^3}+\frac{\delta_2}{\rho R_0^2}\right)x^2+\frac{3\Gamma\delta_1}{\phi\rho R_0^2}x^3=\frac{P_s\lambda\omega}{\phi\rho R_0^2}\cos\omega t. \quad (17)$$

From Eq. (17), the charged bubble equation(3) for the case where $G=0$ Pa can be written in dimensionless form as

$$\ddot{x}+\dot{x}\left[\alpha_0+\alpha_1 x+\alpha_2 x^2+\alpha_3 x^3\right]+\frac{3}{2\phi}\dot{x}^2(1-x+x^2)+\frac{\lambda}{2\phi}\dot{x}^3(1-x+x^2)+\gamma_1 x+\gamma_2 x^2+\gamma_3 x^3=\frac{P_s\lambda\omega}{\phi\rho R_0^2}\cos\omega t-\frac{P_s}{\phi\rho R_0^2}\sin\omega t, \quad (18)$$

where the parameters $\alpha_i(i=0-3)$ and $\gamma_i(i=1-3)$ are

$$\alpha_0=\frac{\lambda}{\phi\rho R_0^2}(1-3\Gamma)\left(\frac{2\sigma}{R_0}-\frac{q^2}{8\pi\epsilon R_0^4}\right)-\frac{3\Gamma\lambda}{\phi\rho R_0^2}(P_0-P_v)-\frac{3q^2\lambda}{8\pi\epsilon\phi\rho R_0^6}+\frac{4\eta}{\phi\rho R_0^2}-\frac{P_s\lambda}{\phi\rho R_0^2}\sin\omega t,$$
$$\alpha_1=-\frac{\lambda}{\phi\rho R_0^2}(1-9\Gamma^2)\left(\frac{2\sigma}{R_0}-\frac{q^2}{8\pi\epsilon R_0^4}\right)+\frac{9\Gamma^2\lambda}{\phi\rho R_0^2}(P_0-P_v)+\frac{15q^2\lambda}{8\pi\epsilon\phi\rho R_0^6}-\frac{8\eta}{\phi\rho R_0^2}+\frac{P_s\lambda}{\phi\rho R_0^2}\sin\omega t,$$
$$\alpha_2=\frac{\lambda}{\phi\rho R_0^2}(1-9\Gamma^2)\left(\frac{2\sigma}{R_0}-\frac{q^2}{8\pi\epsilon R_0^4}\right)-\frac{9\Gamma^2\lambda}{\phi\rho R_0^2}(P_0-P_v)-\frac{45q^2\lambda}{8\pi\epsilon\phi\rho R_0^6}+\frac{12\eta}{\phi\rho R_0^2}-\frac{P_s\lambda}{\phi\rho R_0^2}\sin\omega t,$$
$$\alpha_3=-\frac{3\Gamma\lambda}{\phi\rho R_0^2}(1-3\Gamma)\left(P_0-P_v+\frac{2\sigma}{R_0}-\frac{q^2}{8\pi\epsilon R_0^4}\right), \quad (19)$$

$$\gamma_1=\frac{1}{\phi\rho R_0^2}(1+3\Gamma)\left(\frac{2\sigma}{R_0}-\frac{q^2}{8\pi\epsilon R_0^4}\right)+\frac{3\Gamma}{\phi\rho R_0^2}(P_0-P_v)+\frac{5q^2}{8\pi\epsilon\phi\rho R_0^6}-\frac{4\sigma}{\phi\rho R_0^3}-\frac{P_s}{\phi\rho R_0^2}\sin\omega t,$$
$$\gamma_2=-\frac{1}{\phi\rho R_0^2}(1+3\Gamma)\left(\frac{2\sigma}{R_0}-\frac{q^2}{8\pi\epsilon R_0^4}\right)-\frac{3\Gamma}{\phi\rho R_0^2}(P_0-P_v)-\frac{15q^2}{8\pi\epsilon\phi\rho R_0^6}+\frac{6\sigma}{\phi\rho R_0^3}+\frac{P_s}{\phi\rho R_0^2}\sin\omega t,$$
$$\gamma_3=\frac{3\Gamma}{\phi\rho R_0^2}(1-3\Gamma)\left(P_0-P_v+\frac{2\sigma}{R_0}-\frac{q^2}{8\pi\epsilon R_0^4}\right). \quad (20)$$

Finally, using equations (19) and (20) expressed in terms of the potential $V(x,t)$ of the charged bubble, we obtain

$$\ddot{x}+\dot{x}\left[\alpha_0+\alpha_1 x+\alpha_2 x^2+\alpha_3 x^3\right]+\frac{3}{2\phi}\dot{x}^2(1-x+x^2)+\frac{\lambda}{2\phi}\dot{x}^3(1-x+x^2)+\frac{dV(x,t)}{dx}=\frac{P_s\lambda\omega}{\phi\rho R_0^2}\cos\omega t-\frac{P_s}{\phi\rho R_0^2}\sin\omega t, \quad (21)$$

Appendix 2 - Simulink Model

A block diagram of the charged bubble model (Eq. (9)) was designed in MATLAB-Simulink and is shown in Figure 19. Subsystem 1 in Figure 19 has input 1 and input 2 as $1/x$ and y, respectively and an output that performs $z_1\left(1+z_2 y\right)/x^{3\Gamma}$. Subsystem 2 in Figure 19 has an input y, output 2 as y/c and an output 1 that performs $\frac{y^2}{2}\left(3-\frac{y}{c}\right)$. For subsystem 3, input 1, input 2 and output 2 are $1/x$, y/c and 1, respectively. Output 1 performs $\frac{z_3}{x^4}\left(1-\frac{3y}{c}\right)$. Subsystem 4 has input 1, input 2, output 1 and output 2 as $1/x$, y, z_4/x and $z_5 y/x$, respectively.

Subsystem 5 has input 1, input 2, input 3 and input 4 as 1, $\sin\omega t$, y/c and $1+G\sin\Omega t$, respectively and an output that performs $\Delta_1(t)\left(1+\frac{y}{c}\right)$. Subsystem 6 has input 1,

input 2, input 3, input 4 and input 5 as ωt, $\sin\omega t$, $\cos\Omega t$, $1 + G\sin\Omega t$ and x, respectively and an output that performs $x\Delta_2(t)$. The input 1, input 2 and input 3 on subsystem 7 are y/c, 1 and x, respectively; while it has an output that performs $\left(1 - \frac{y}{c}\right)x + z_{10}$. Subsystem 8 is a time-function block with 1 as the only input, and output 1, output 2, output 3 and output 4 perform $\sin\omega t$, ωt, $1 + G\sin\Omega t$ and $G\cos\Omega t$ respectively.

References

[1] Lord Rayleigh, VIII. On the pressure developed in a liquid during the collapse of a spherical cavity, Philos. Mag. 34 (1917) 94–98.

[2] W. Lauterborn, T. Kurz, Physics of bubble oscillations, Rep. Prog. Phys. 73 (2010) 106501.

[3] U. E. Vincent, O. Kolebaje, Introduction to the dynamics of driven nonlinear systems, Contemp. Phys. 61 (2020) 169–192.

[4] V. S. Anishchenko, T. E. Vadivasova, G. I. Strelkova, Deterministic Nonlinear Systems, 1st ed., Springer-Verlag Berlin Heidelberg, Germany, 2014.

[5] O. I. Olusola, O. P. Shomotun, U. E. Vincent, P. V. E. McClintock, Quantum vibrational resonance in a dual-frequency driven Tietz-Hua quantum well, Phys. Rev. E 101 (2020) 052216.

[6] M. Gitterman, The noisy oscillator: random mass, frequency, damping, 2 ed., World Scientific, Singapore, 2013.

[7] M. Ashokkumar, The characterization of acoustic cavitation bubbles–an overview, Ultrason. Sonochem. 18 (2011) 864–872.

[8] K. A. Omoteso, T. O. Roy-Layinde, J. A. Laoye, U. E. Vincent, P. V. E. McClintock, Acoustic vibrational resonance in a Rayleigh-Plesset bubble oscillator, Ultrason. Sonochem. 71 (2020) 105346.

[9] X. Han, Q. Bi, P. Ji, J. Kurths, Fast-slow analysis for parametrically and externally excited systems with two slow rationally related excitation frequencies, Phys. Rev. E 92 (2015) 012911.

[10] X. Han, F. Xia, C. Zhang, Y. Yu, Origin of mixed-mode oscillations through speed escape of attractors in a Rayleigh equation with multiple-frequency excitations, Nonlinear Dyn. 88 (2017) 2693–2703.

[11] X. Han, Y. Liu, Q. Bi, J. Kurths, Frequency-truncation fast-slow analysis for parametrically and externally excited systems with two slow incommensurate excitation frequencies, Commun. Nonlin. Sci. Numer. Simulat. 72 (2019) 16–25.

[12] K. S. Oyeleke, O. I. Olusola, O. T. Kolebaje, U. E. Vincent, A. B. Adeloye, P. V. E. McClintock, Novel bursting oscillations in a nonlinear gyroscope oscillator, Phys. Scr. 97 (2022) 085211.

[13] Y. Zhang, S. Li, Combination and simultaneous resonances of gas bubbles oscillating in liquids under dual-frequency acoustic excitation, Ultrason. Sonochem. 35 (2017) 431–439.

[14] K. A. Omoteso, T. O. Roy-Layinde, J. A. Laoye, U. E. Vincent, P. V. E. McClintock, Delay-induced vibrational resonance in the Rayleigh-Plesset bubble oscillator, J. Phys. A: Math. Theor. 55 (2022) 495701.

[15] Y. Zhang, Rectified mass diffusion of gas bubbles in liquids under acoustic field with dual-frequencies, Int. Commun. Heat Mass 39 (2012) 1496–1499.

[16] Z. Li, Q. Zou, D. Qin, Enhancing cavitation dynamics and its mechanical effects with dual-frequency ultrasound, Phys. Med. Biol. 67 (2022) 085017.

[17] F. Hegedüs, K. Klapcsik, W. Lauterborn, U. Parlitz, R. Mettin, GPU accelerated study of a dual-frequency driven single bubble in a 6-dimensional parameter space: The active cavitation threshold, Ultrason. Sonochem. 67 (2020) 105067.

[18] L. Ye, X. Zhu, Y. He, T. Song, Effect of frequency ratio and phase difference on the dynamic behavior of a cavitation bubble induced by dual-frequency ultrasound, Chem. Eng. Process. 165 (2021) 108448.

[19] C. Bian, H. Yu, K. Yang, J. Mei, J. Xie, Effects of single-, dual-, and multi-frequency ultrasound-assisted freezing on the muscle quality and myofibrillar protein structure in large yellow croaker (Larimichthys crocea), Food Chem. X 15 (2022) 100362.

[20] H. A. McTaggart, XXXIII. The electrification at liquid-gas surfaces, Philos. Mag. 27 (1914) 297–314. doi:10.1080/14786440208635092.

[21] T. Alty, The origin of the electrical charge on small particles in water, Proc. Roy. Soc. Lond. A 112 (1926) 235–251. doi:10.1098/rspa.1926.0108.

[22] T. Alty, The cataphoresis of gas bubbles in water, Proc. Roy. Soc. Lond. A 106 (1924) 315–340.

[23] H.-B. Lee, P.-K. Choi, Electrification of sonoluminescing single bubble, J. Phys. Chem. B 124 (2020) 3145–3151. doi:10.1021/acs.jpcb.0c00956.

[24] A. Pelesz, Charging of a single soap bubble, Prz. Eleck. 94 (2018) 176–179.

[25] S. S. Dastgheyb, J. R. Eisenbrey, Microbubble applications in biomedicine, in: K. Modjarrad, S. Ebnesajjad (Eds.), Handbook of Polymer Applications in Medicine and Medical Devices, volume 11 of *Plastics Design Library*, William Andrew Publishing, Oxford, 2014, pp. 253–277.

[26] A. J. Atkinson, O. G. Apul, O. Schneider, S. Garcia-Segura, P. Westerhoff, Nanobubble technologies offer opportunities to improve water treatment, Acc. Chem. Res. 52 (2019) 1196–1205.

[27] K. K. Thi Phan, T. Truong, Y. Wang, B. Bhandari, Nanobubbles: Fundamental characteristics and applications in food processing, Trends Food Sci. Tech. 95 (2020) 118–130.

[28] T. Hongray, B. Ashok, J. Balakrishnan, Effect of charge on the dynamics of an acoustically forced bubble, Nonlinearity 27 (2014) 1157–1179.

[29] T. Hongray, B. Ashok, J. Balaskrishan, Oscillatory dynamics of a charged microbubble under ultrasound, Pramana - J. Phys. 84 (2015) 517–541.

[30] B. Ashok, T. Hongray, J. Balakrishnan, The charged bubble oscillator: Dynamics and thresholds, in: R. Sagar (Ed.), Proceedings of the Conference on Perspectives in Nonlinear Dynamics, volume 1 of *Conference Series*, Indian Academy of Sciences, Indian Academy of Sciences, India, 2017, pp. 109–115.

[31] U. E. Vincent, P. V. E. McClintock, I. A. Khovanov, S. Rajasekar, Vibrational and stochastic resonances in driven nonlinear systems, Phil. Trans. Roy. Soc. A 379 (2021) 20200226.

[32] P. S. Landa, P. V. E. McClintock, Vibrational resonance, J. Phys. A: Math. Gen. 33 (2000) L433.

[33] M. Gosak, M. Perc, S. Kralj, The impact of static disorder on vibrational resonance in a ferroelectric liquid crystal, Mol. Cryst. Liq. Cryst. 553 (2012) 13–20. doi:10.1080/15421406.2011.609343.

[34] S. Rajasekar, M. A. F. Sanjuán, Nonlinear Resonances, Springer Series in Synergetics, Springer, Switzerland, 2016.

[35] U. E. Vincent, T. O. Roy-Layinde, P. O. Adesina, O. O. Popoola, P. V. E. McClintock, Vibrational resonance in an oscillator with an asymmetrical deformable potential, Phys. Rev. E 98 (2018) 062203.

[36] S. Paul, D. Shankar Ray, Vibrational resonance in a driven two-level quantum system, linear and nonlinear response, Phil. Trans. Roy. Soc. A 379 (2021) 20200231.

[37] P. Sarkar, S. Paul, D. S. Ray, Subharmonics and superharmonics of the weak field in a driven two-level quantum system: Vibrational resonance enhancement, Phys. Rev. E 104 (2021) 014202.

[38] T. O. Roy-Layinde, U. E. Vincent, S. A. Abolade, O. O. Popoola, J. A. Laoye, P. V. E. McClintock, Vibrational resonances in driven oscillators with position-dependent mass, Phil. Trans. R. Soc. A 379 (2021) 20200227.

[39] U. E. Vincent, P. V. E. McClintock, I. A. Khovanov, S. Rajasekar, Vibrational and stochastic resonance in driven nonlinear systems, Phil. Trans. R. Soc. A 379 (2021) 20200226.

[40] U. E. Vincent, P. V. E. McClintock, I. A. Khovanov, S. Rajasekar, Vibrational and stochastic resonance in driven nonlinear systems - part two, Phil. Trans. R. Soc. A 379 (2021)

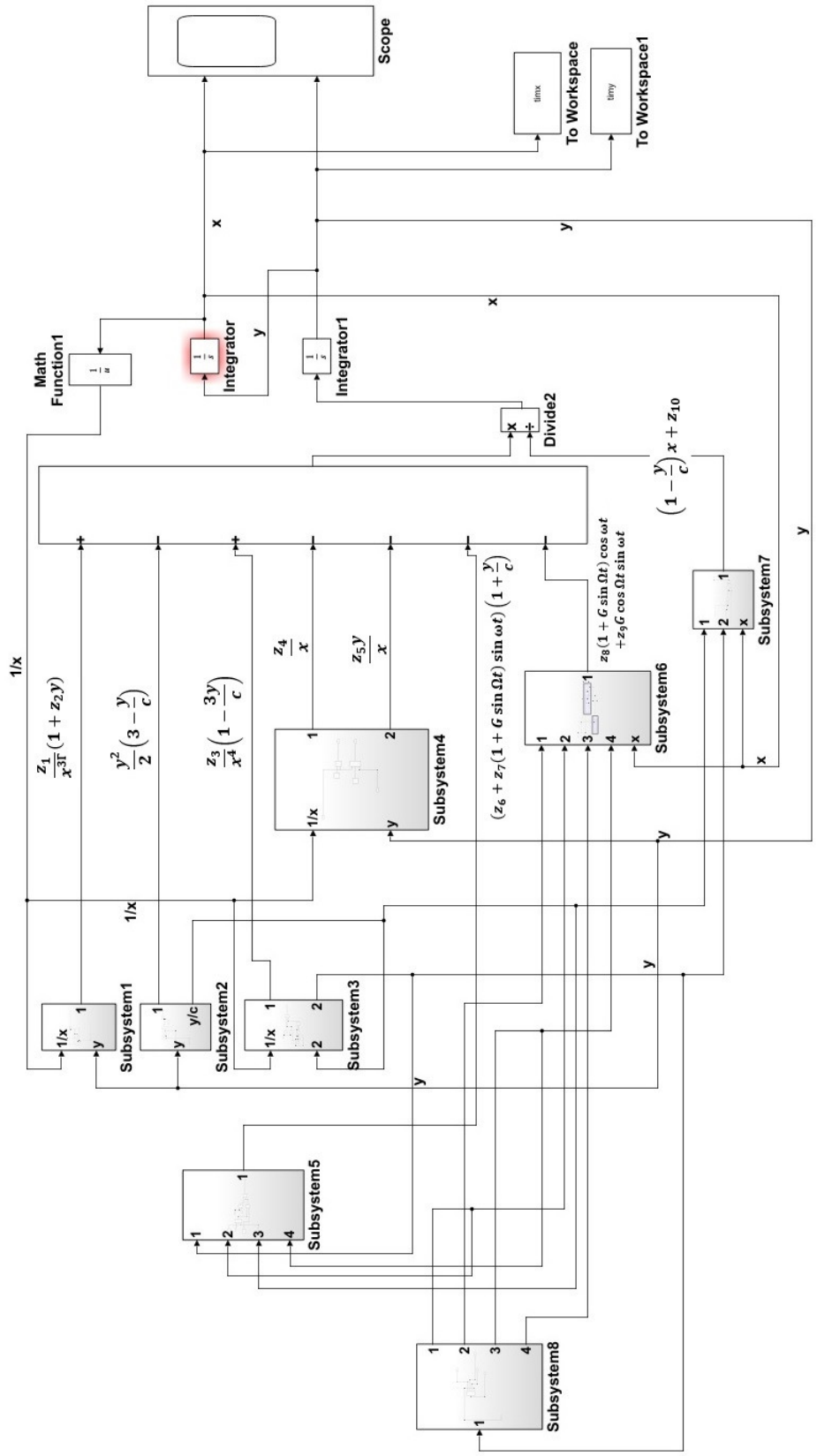

Figure 19: Simulink implementation of the charged bubble oscillator model.

20200226.
[41] K. S. Oyeleke, O. I. Olusola, U. E. Vincent, D. Ghosh, P. V. E. McClintock, Parametric vibrational resonance in a gyroscope driven by dual-frequency forces, Phys. Lett. A 387 (2021) 127040.
[42] L. Xiao, R. Bajric, J. Zhao, J. Tang, X. Zhang, An adaptive vibrational resonance method based on cascaded varying stable-state nonlinear systems and its application in rotating machine fault detection, Nonlinear Dyn.170 103 (2021) 715–739. doi:10.1007/s11071-020-06143-y.
[43] C. Ainamon, L. Hinvi, F. C. Patinvoh, A. V. M. Clément Hodévéwan Miwadinou, J. B. C. Orou, Influence of amplitude-modulated excitation on the dynamic behaviour of polarisation of a material, Pramana - J. Phys. 95 (2021) 170. doi:10.1007/s12043-021-02168-z.
[44] O. Kolebaje, O. Popoola, U. Vincent, Occurrence of vibrational resonance in an oscillator with an asymmetric toda potential, Physica D 419 (2021) 132853. doi:10.1016/j.physd.2021.132853.
[45] J. Jiang, K. Li, W. Guo, L. Du, Energetic and entropic vibrational resonance, Chaos, Solitons & Fractals 152 (2021) 111400. doi:10.1016/j.chaos.2021.111400.
[46] T. Gong, J. Yang, M. A. F. Sanjuán, H. Liu, Z. Shan, Vibrational resonance by using a real-time scale transformation method, Phys. Scr. 97 (2022) 045207. doi:10.1007/s11071-020-06143-y.
[47] T. O. Roy-Layinde, K. A. Omoteso, B. A. Oyero, J. A. Laoye, U. E. Vincent, Vibrational resonance of ammonia molecule with doubly singular position-dependent mass, Eur. Phys. J. B 95 (2022) 80.
[48] I. S. Sawkmie, D. Kharkongor, Theoretical and numerical study of vibrational resonance in a damped softening Duffing oscillator, Int. J. Non-Linear Mech. 144 (2022) 104055. doi:10.1016/j.ijnonlinmec.2022.104055.
[49] G. Madiot, S. Barbay, R. Braive, Vibrational resonance amplification in a thermo-optic optomechanical nanocavity, Nano Lett. 21 (2021) 8311–8316. doi:10.1021/acs.nanolett.1c02879.
[50] M. Lakshmanan, V. K. Chandrasekar, Generating finite dimensional integrable nonlinear dynamical systems, Eur. Phys. J. Spec. Top. 222 (2013) 665–688.
[51] S. Behnia, A. J. Sojahrood, W. Soltanpoor, O. Jahanbakhsh, Suppressing chaotic oscillations of a spherical cavitation bubble through applying a periodic perturbation, Ultrason. Sonochem. 16 (2009) 502 – 511.
[52] A. I. Grigor'ev, A. N. Zharov, Stability of the equilibrium states of a charged bubble in a dielectric liquid, Tech. Phys. 45 (2000) 389–395.
[53] Y. Zhang, Analysis of radial oscillations of gas bubbles in Newtonian or viscoelastic mediums under acoustic excitation, PhD Thesis, University of Warwick, Warwick, UK, 2012.
[54] F. Hamaguchi, K. Ando, Linear oscillation of gas bubbles in a viscoelastic material under ultrasound irradiation, Phys. Fluids 27 (2015) 113103 (1–17).
[55] D. Young, B. Munson, T. Okiishi, W. Huebsch, A Brief Introduction to Fluid Mechanics., 5th ed., John Wiley & Sons., 2010.
[56] W. Graebel, Engineering Fluid Mechanics, Taylor & Francis, 2001.
[57] J. J. Deng, R. F. Yang, H. Q. Lu, Dynamics of nonspherical bubble in compressible liquid under the coupling effect of ultrasound and electrostatic field, Ultrason. Sonochem. 71 (2021) 105371. doi:10.1016/j.ultsonch.2020.105371.
[58] W. Lauterborn, Numerical investigation of nonlinear oscillations of gas bubbles in liquids, J. Acoust. Soc. Am. 59 (1976) 283–293.
[59] T. R. Stottlemyer, R. E. Apfel, The effects of surfactant additives on the acoustic and light emissions from a single stable sonoluminescing bubble, J. Acoust. Soc. Am. 102 (1997) 1418–1423.
[60] M. Keswani, S. Raghavan, P. Deymier, Effect of non-ionic surfactants on transient cavitation in a megasonic field, Ultrason. Sonochem. 20 (2013) 603–609.
[61] H. Wu, H. Zheng, Y. Li, C.-D. Ohl, H. Yu, D. Li, Effects of surface tension on the dynamics of a single micro bubble near a rigid wall in an ultrasonic field, Ultrason. Sonochem. 78 (2021) 105735.
[62] A. Pelesz, P. Zylka, On analytical and experimental aspects of soap bubble stream charging, Exp Fluids 61 (2020) 241.
[63] T. D. Dinh, J.-W. Jang, S. Hwang, Long-range electrification of an air/electrolyte interface and probing potential of zero charge by conductive amplitude-modulated atomic force microscopy, Anal. Chem. 95 (2023) 2901–2908.
[64] N. Yadav, P. Sen, A. Ghosh, Bubbles in superfluid helium containing six and eight electrons: Soft, quantum nanomaterial, Sci. Adv. 7 (2021) eabi7128.
[65] C. R. Heckman, R. H. Rand, Dynamics of microbubble oscillators with delay coupling, Nonlinear Dyn. 71 (2013) 121–132.
[66] F. Hegedűs, Topological analysis of the periodic structures in a harmonically driven bubble oscillator near Blake's critical threshold: Infinite sequence of two-sided Farey ordering trees, Phys. Lett. A 380 (2016) 1012–1022.
[67] F. Hegedűs, C. Hős, L. Kullmann, Stable period 1, 2 and 3 structures of the harmonically excited Rayleigh–Plesset equation applying low ambient pressure, IMA J. Appl. Math. 78 (2013) 1179–1195.